Investigation of Singlet Fission Mechanisms in Carotenoid Dimers



George Alexander Smith

Worcester College

A thesis submitted for the Honour School of Chemistry

Part II 2026

I dedicate this thesis to Yuan, my dearest love.
You are my brightest inspiration.
Thank you for your warmth and care always.

Acknowledgements

I would like to thank Prof. William Barford for his attentive guidance and vast knowledge, from which I have attempted to acquire a fraction.

To the Worcester chemists — Ariana, Brad, Eirinn, Ellie, Manami, Reyati, Sam, and Susanna. Thank you all for your companionship over the last four years.

To the Barford group, thank you for building a welcoming and intellectually nourishing environment. Thank you, Alex, for your close supervision and ability to steer me onto the right track. Thank you, Tim and Louis, for listening to my frustrations with uncooperative code.

Thank you to my family who have always trusted and supported me in achieving my dreams.

I acknowledge the use of ChatGPT 5 Edu for the purposes of reformatting Python plotting scripts and segments of FORTRAN code.

Summary

Singlet fission is a photophysical process that has recently seen intense investigation for applications in next generation high efficiency solar cell materials. In this thesis, we present a reduced basis low energy model of the π-electron states in polyenes and use it to investigate potential mechanisms of singlet fission in carotenoids.

In Chapter 1, we introduce the singlet fission process, describe its application in solar technology, and discuss current mechanistic understanding of the process.

Chapter 2 begins by introducing the Pariser-Parr-Pople (PPP) Hamiltonian from which we construct our simplified polyene model. We describe the basis states and matrix elements that are included in our model and how symmetry-breaking terms allow us to model dynamical processes. Finally, we present the Redfield equation which is used to simulate dynamics in the presence of an (external) environment.

Chapter 3 explains the computational methods used in this thesis. We briefly discuss the Density Matrix Renormalisation Group (DMRG) approach to exactly solving the PPP Hamiltonian and then explain the Arnoldi iteration method for integrating the secular Redfield equation.

Chapter 4 discusses the DMRG results for a single chain and a model dimer and how our reduced basis model is parameterised against them.

Chapter 5 presents the dynamical results of our model under unitary evolution and Redfield dissipation, along with the effects of symmetry breaking terms on the population of states relevant to singlet fission.

Finally, in Chapter 6 we present the conclusions drawn from our model calculations and provide suggestions for further investigation of singlet fission in carotenoids.

Contents

Glossary and Abbreviations **xi**

1 Introduction **1**
1.1 Singlet Fission . . . 1
1.2 Proposed Mechanisms of Singlet Fission . . . 2
1.2.1 Polyacenes . . . 3
1.2.2 Polyenes . . . 3
1.2.3 Carotenoids . . . 5

2 Theoretical Background **9**
2.1 Carotenoid Electronic Structure . . . 9
2.1.1 Pariser-Parr-Pople Theory . . . 9
2.1.2 Symmetries of Carotenoids . . . 11
2.1.3 The Nature of Carotenoid Excited States . . . 12
2.2 The Model Hamiltonian and Basis . . . 13
2.2.1 Single-chain Hamiltonian . . . 13
2.2.2 Aggregate Hamiltonian . . . 18
2.2.3 Symmetry Breaking . . . 23
2.2.4 Vibronic Coupling . . . 24
2.3 Time Evolution . . . 25
2.3.1 Liouville-von Neumann Equation . . . 25
2.3.2 The Redfield Equation . . . 26

3 Computational Methods **27**
3.1 Density Matrix Renormalisation Group . . . 27
3.2 Short Iterative Arnoldi Propagator . . . 28

4 Model Parameterisation **31**
4.1 Single chain model . . . 31
4.2 Dimer Model . . . 35

5 Dynamics Simulations **41**
5.1 Unitary Evolution . . . 41
5.1.1 Breaking Particle-Hole Symmetry . . . 41
5.1.2 Breaking Spatial Symmetry . . . 42
5.1.3 Vibronic Coupling . . . 46
5.2 Dissipative Dynamics . . . 47
5.2.1 Vibronic Coupling . . . 48
5.2.2 Breaking Spatial Symmetry . . . 49

6 Conclusions **51**

Bibliography **53**

Appendices

A Solution of the PPP Hamiltonian for Ethylene **61**

B Super-Exchange Triplet Hopping **63**

C Character Table for the C_{2h} Point Group **65**

D The Redfield Equation **67**

D.0.1 Redfield Equation 68

D.0.2 The Secular Approximation 69

Glossary and Abbreviations

BChl . . . . . Bacteriochlorophyll.

Carotenoid dimer . . Two closely spaced, interacting carotenoid chains.

CT . . . . . Charge-transfer. Used to refer to interchain charge-transfer basis states.

DFT . . . . . Density functional theory.

DMRG . . . . . Density matrix renormalisation group.

EPR . . . . . Electron paramagnetic resonance spectroscopy.

EX . . . . . Intrachain charge-transfer exciton basis state.

FE . . . . . Frenkel exciton. An electron-hole excitation confined to one ethylene unit within a polyene.

FSRS . . . . . Femtosecond stimulated Raman spectroscopy.

H-aggregate . . . . . Aggregates which have a blue-shifted absorption spectrum relative to their monomer.

HOMO . . . . . Highest occupied molecular orbital.

iTT . . . . . A triplet-pair basis state with both triplets confined to a single molecule or an intrachain triplet-pair eigenstate such as $2^1A_g^-$.

J-aggregate . . . . . Aggregates which have a red-shifted absorption spectrum relative to their monomer.

LUMO . . . . . Lowest unoccupied molecular orbital.

MO . . . . . Molecular orbital.

PH . . . . . Particle-hole symmetry.

PPP . . . . . Pariser-Parr-Pople theory.

SF . . . . . Singlet fission.

TA . . . . . Transient absorption spectroscopy.

TT . . . . . A pair of triplets on separate molecules.

TTA . . . . . Triplet-triplet annihilation. The reverse process to singlet fission.

TRRR . . . . . Time-resolved resonance-Raman spectroscopy.

1 Introduction

1.1 Singlet Fission

Solar radiation is the most plentiful source of renewable energy, but the efficient conversion of sunlight into electricity remains a strong challenge. The Shockley-Queisser thermodynamic limit of the efficiency of a single-junction silicon solar cell is 30%[1], with the principal losses being due to the inability to absorb photons with $E < E_g$ (band gap) and the thermalisation of high energy photons with $E > E_g$. Recent research has proposed to overcome the latter issue by utilising a singlet fission (SF) sensitiser material, in tandem with a conventional silicon chromophore, which can convert one high energy singlet exciton into two lower energy triplet excitons (with $E_T \approx E_g$) that can subsequently be harvested[2]. Despite SF first being observed in the early 1960s[3], it was not until the mid-2000s that theoretical work[4] demonstrated its potential to raise the Shockley-Queisser limit up to 44%. This has sparked a growing interest in SF materials[5, 6].

A simple mechanism for singlet fission may be written as[7],

$$\mathrm{S_0 + S_0} \xrightarrow{h\nu} \mathrm{S_1 + S_0} \rightarrow {}^1\mathrm{(TT)} \rightarrow \mathrm{T_1 + T_1}, \tag{1.1}$$

where the initial photo-excited $\mathrm{S_1}$ state couples to another molecule in its ground state forming the triplet-pair state, ${}^1\mathrm{(TT)}$, made up of two entangled triplet excitons on different molecules coupled into an overall singlet, making the process spin-allowed.

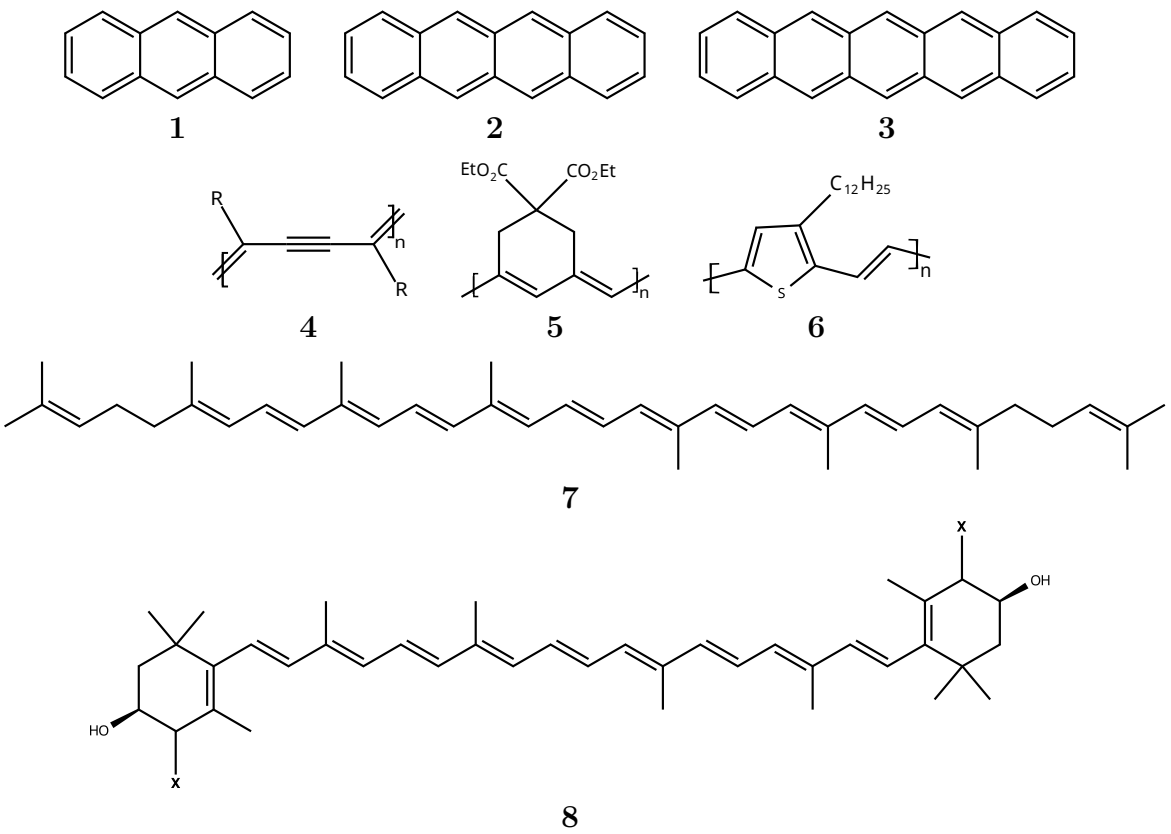


Figure 1.1: Structures of singlet fission materials referred to in this thesis.

The ^{1}(TT) state then loses spin and electronic coherence, forming two independent triplets. Therefore, the principal conditions for rapid SF are for $E(S_1) \geq 2E(T_1)$ and for the electronic coupling between S_1 and ^{1}(TT) to be strong. Additionally, we should want the reverse process of triplet-triplet annihilation (TTA) to be slow.

It has been found that these conditions are rather strict and thus SF has been observed in only a few classes of molecules such as polyacenes, polyenes, and carotenoids[5]. Notable examples of these are shown in Figure 1.1.

1.2 Proposed Mechanisms of Singlet Fission

A good understanding of the microscopic mechanism of SF beyond the simplified ideas of equation 1.1 may help us to develop better design principles for new SF materials. No single unified mechanism has been shown to apply to all SF chromophores and there are ongoing controversies in the literature between competing mechanisms.

In this section, we discuss the experimental evidence and theoretical proposals for mechanisms of singlet fission in the key classes of materials.

1.2.1 Polyacenes

Understanding of singlet fission is most advanced in polyacenes. SF was first observed in anthracene (**1**) crystals[3], where it is slightly endergonic, and has subsequently been observed in the longer acenes, tetracene (**2**) and pentacene (**3**), on shorter timescales and with greater exergonicity leading to higher triplet yields. An early explanation of the SF process was given by Swenberg[8] who suggested two potential pathways; the first of these is a direct Coulomb-driven coupling between S_1 and ^{1}(TT) (Fig. 1.2a) and the second being mediated by a charge-transfer (CT) state in which an electron has been transferred from the molecule in its S_1 state to a neighbouring molecule in its ground state. This latter mechanism itself comes in several flavours; a superexchange type mechanism where both the initial S_1 state and the final ^{1}(TT) are mixed with a high-lying CT state which virtually couples the two states (Fig. 1.2b), and a second type where the CT state is a real populated intermediate that lies energetically between the two states (Fig. 1.2c). The current consensus favours the CT-mediated mechanism in most materials[9, 10]. However, the nature of the CT state has been shown to be quite sensitive to side-groups and crystal structure[11].

1.2.2 Polyenes

Extended π-conjugated systems, such as those in polyenes, introduce additional complexities due to the presence of dark excited covalent singlet states (such as $2^1A_g^-$, $1^1B_u^-$, and $3^1A_g^-$) that lie lower in energy than the ionic bright state (now S_2) but are optically inaccessible. These dark states are considered to be intramolecular bound triplet-pairs, made up of two triplet excitations coupled into an overall singlet state.

The manifold of dark states therefore presents a potential alternative pathway

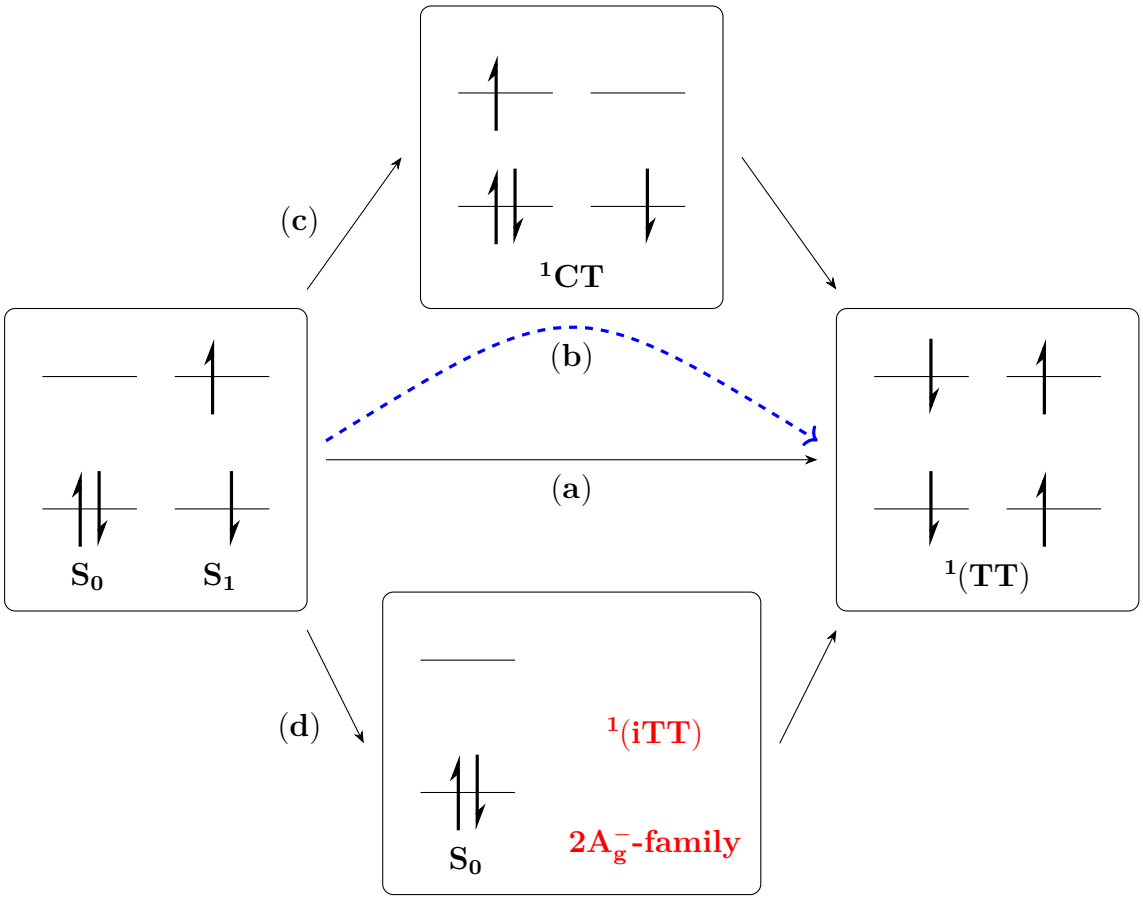


Figure 1.2: Proposed mechanisms of singlet fission. a) Direct $S_1 - {}^1(TT)$ coupling, b) CT superexchange, c) Explicit CT intermediate, d) Dark-state mediated pathway.

for singlet fission (Fig. 1.2d) where the initial S_2 state is localised on a molecule and then undergoes internal conversion into an intramolecular triplet-pair state, ^{1}(iTT), which may subsequently unbind, decohere, and diffuse to form independent triplet excitations[12]. This mechanism has been suggested in polydiacetylenes[13] (**4**) and long-chain oligoenes[14] (**5**) where it has been claimed that a length of 20 double bonds is the minimum for triplet-pairs to be able to separate. This process is expected to be relevant for systems with strong $S_2{-}{}^1$(iTT) coupling and $E(^1(\text{iTT})) \geq 2E(T_1)$. On the other hand, it has been argued that in some polymers, such as (**6**), the mechanism is more similar to acenes, with the S_2 state decaying directly into a triplet-pair without involving the $2^1A_g^-$ state[15]. However, recent investigation has reinforced the dark state mediation in (**6**) by explaining the absence of the $2^1A_g^-$ signal by invoking the higher-lying $3^1A_g^-$ triplet-pair state as the intermediate[16].

1.2.3 Carotenoids

Carotenoids are naturally-occurring tetraterpenoid derivatives that exhibit similar optical properties to conjugated polymers due to their common extended π-electron backbone. In nature, they play an important role in photoprotection during photosynthesis[17] and their interesting photochemical properties have been investigated for numerous technological uses[18, 19]. Carotenoids are the only known system where singlet fission can occur in both biological material[20–22] and synthetic aggregates[23]. Although carotenoids are not currently being investigated for use in solar cells, molecules with similar electronic structure such as diphenylhexatriene (**9**) are under investigation[24]. An understanding of the mechanism in this class of chromophore is then important for both theoretical and technological reasons, but has proven controversial and unrevealing.

1.2.3.1 Intramolecular Singlet Fission

Due to the shorter conjugation length in carotenoids compared with long-chain polyenes, intramolecular singlet fission is expected to be far less favourable. For some time, it was considered possible in certain biological structures, such as the bacteriochlorophyll-carotenoid (BChl-Car) complex in purple photosynthetic bacteria, where the carotenoid is twisted so that conjugation breaks and the system can accommodate two uncorrelated triplets[25]. This interpretation has recently been questioned by investigation of an orange carotenoid protein system which has both a twisted and a planar form, neither of which exhibits singlet fission[26]. The BChl-Car intramolecular SF proposal has since been reinterpreted as a heterofission process involving formation of a $^1(TT)$ state across both constituents of the BChl-Car complex, which forms the first step in an SF-mediated energy-transfer step relevant to photosynthesis[27].

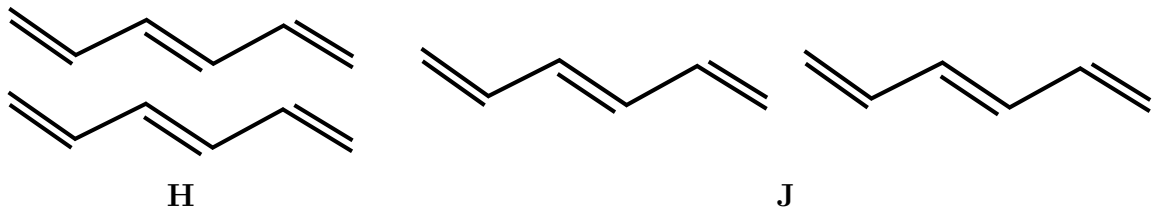


Figure 1.3: Geometries of H- and J-aggregates of carotenoids.

1.2.3.2 Intermolecular Singlet Fission

Singlet fission in carotenoids is then an intrinsically intermolecular process but the nature of the mechanism is complicated by the additional manifold of intramolecular dark triplet-pair states that may be rapidly accessed from the bright state.

SF has been most investigated in aggregates of carotenoids, which can exist between two extremes of morphology called H- and J-aggregates (Fig. 1.3). The morphology is assigned based on the sign of the dipole-dipole coupling induced shift in absorption upon aggregation, with H-aggregates showing a blue-shift and reduced fluorescence while J-aggregates are red-shifted (Fig. 1.4) relative to the monomer absorption. This concept has been developed further by considering the additional effects of intermolecular electron transfer which, depending on the sign of overlaps, may oppose or reinforce the dipolar splitting (as we discuss later in Section 2.2.2). In cases of strong intermolecular coupling, it is therefore better to use terminology such as hJ-aggregate where the first letter describes the effect of the (long range) dipolar coupling, the second describes the (short range) electron transfer effect, and the capital indicates which effect is dominant[28].

Time-resolved resonance-Raman (TRRR) and transient absorption (TA) spectroscopy have been used to study SF processes in carotenoid aggregates. Wang, Tauber and coworkers found no evidence of an intermediate (within 300 fs) between the decay of the bright S_2 state and the rise of the triplet signal in zeaxanthin (**8**, X=H) aggregates of varying morphologies[23, 29, 30]. Further studies of astaxanthin

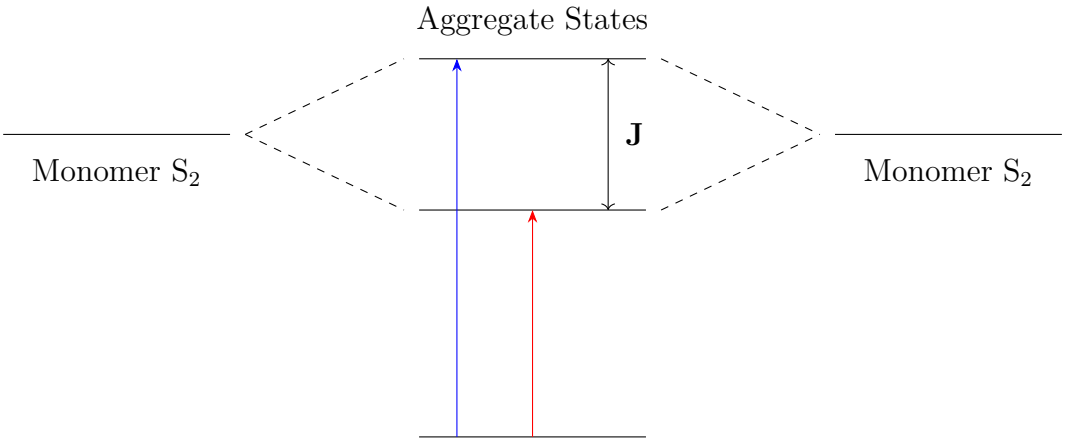


Figure 1.4: Dipole-allowed transitions of H- (blue) and J-aggregates (red) where J is the splitting due to dipolar coupling.

(**8**,X=Carbonyl) aggregates also suggested a direct mechanism (Fig. 1.2a) with singlet fission time constants as short as 65 fs and, crucially, complete deactivation of the monomeric S_1 decay pathway[31]. Some theoretical calculations have suggested these observations could only be explained by CT mediation (as in polyacenes) due to the smaller predicted $S_2 - {}^1(TT)$ coupling compared with $S_2 - CT$ coupling[32]. However, others emphasised the stronger SF potential of iTT states, and suggested conversion via rapid mixing of S_2 with iTT states but only as a pathway towards TT, with no full relaxation into S_1[33]. In other systems, the S_1 signal was still observed in aggregates and was proposed to be the parent state of the triplets[22, 34].

More recent investigations have focused on lycopene (**7**) due to its simple polyene backbone and favourable energetics for SF. Kundu and Dasgupta prepared H-aggregates which were found to produce triplets with a very long lifetime of 440 μs (compared with 13 μs in the monomer)[35]. Their TA experiments indicated the following pathways,

$$\begin{gathered} S_2 \xrightarrow{167\text{ fs}} S^* \xrightarrow{19\text{ ps}} {}^1(TT) \xrightarrow{393\text{ ps}} T + T \rightarrow S_0 \\ S_2 \xrightarrow{167\text{ fs}} S_1 \xrightarrow{4\text{ ps}} S_0, \end{gathered} \tag{1.2}$$

where they observed a spectrally distinct $^1(TT)$ state as well as a long-lived intermediate, S^*, that they tentatively assigned as the $1^1B_u^-$ triplet-pair state. This

aligned with previous work which indicated that higher-lying $2A_g$-family states may spontaneously unbind into separated triplets[36, 37].

Taking $S^* = 1^1B_u^-$ as their initial condition, Barford and Chambers described how interchain triplet-hopping followed by environmental spin-dephasing interactions would allow a correlated intrachain triplet-pair to lose coherence to form independent triplets[38, 39]. Considering exchange and dipolar interactions, Ichert and Barford then predicted a distinct electron paramagnetic resonance (EPR) pattern for triplets produced via this mechanism vs the CT-mediated mechanism[40].

Conversely, using femtosecond stimulated Raman spectroscopy (FSRS) on similarly prepared lycopene H-aggregates, Peng et al. found evidence of charge-transfer build up coincident with the rise and relaxation of S^* not present in monomeric lycopene, casting doubt on the dark-state mechanism[41]. it has since been pointed out that the aggregates in these studies were likely highly heterogeneous, making the assignment of spectroscopic properties to a single species uncertain[42].

The experimental evidence is therefore far from conclusive. Recent qualitative studies have found large couplings along both iTT and CT-mediated pathways in H-aggregates[43] and raised the possibility of the mixing of iTT and CT states joining up the S^* suggestions of [35] and [41]. However, these studies used a small model decapentaene system rather than a real carotenoid and did not investigate time-dependent phenomena so the exact relevance of each mechanism still remains unclear.

In this thesis, we hope to shed some light on this problem by presenting a reduced basis model of lycopene aggregates which we parameterise against exact density matrix renormalisation group (DMRG) calculations of monomeric lycopene and dimers within the Pariser-Parr-Pople (PPP) Hamiltonian. This model system contains representations of all the states and couplings relevant to singlet fission, and is small enough to enable feasible time-dependent mechanistic studies of large aggregate systems.

2
Theoretical Background

2.1 Carotenoid Electronic Structure

The electronic structure of conjugated polymers is a perfect storm of both strong electronic correlation, requiring large multireference calculations, and strong electron-nuclear coupling, requiring explicit treatment of nuclear dynamics for accurate results. In this thesis, our attention is focused primarily on the problem of describing the interacting electrons.

2.1.1 Pariser-Parr-Pople Theory

In 1953, Rudolph Pariser, Robert Parr, and John Pople introduced a theory to describe electron correlation in π-conjugated systems [44–46]. The theory followed from Erich Hückel's description of the energetic separation of σ-bonding and π-bonding [47], whereby the core electrons in a conjugated system are considered to form a screened background above which the π-electron dynamics take place. The model is arrived at by first integrating out both the nuclear (under the Born-Oppenheimer approximation) and σ-electron degrees of freedom, giving the second-quantised form,

$$\hat{H}^{\pi}_{BO} = \sum_{i,j,\sigma} t_{ij}(\hat{c}^{\dagger}_{i\sigma}\hat{c}_{j\sigma} + h.c.) + \frac{1}{2}\sum_{i,j,k,l,\sigma,\sigma'} V^{\text{eff}}_{ijkl}\hat{c}^{\dagger}_{i\sigma}\hat{c}^{\dagger}_{j\sigma'}\hat{c}_{l\sigma'}\hat{c}_{k\sigma}, \tag{2.1}$$

where $\hat{c}^{\dagger}_{i\sigma}$ ($\hat{c}_{j\sigma}$) creates (annihilates) an electron in the p_z-orbital on the ith carbon atom with spin σ. The two- and four-centre integrals are defined under the effective

electron-electron interaction V_{e-e}^{eff} and the electron-nuclear pseudopotential V_p as

$$\begin{aligned} V_{ijkl}^{\text{eff}} &= \int\int d^3\mathbf{r}d^3\mathbf{r}'\ \phi_i^*(\mathbf{r})\phi_j^*(\mathbf{r}')V_{e-e}^{\text{eff}}(\mathbf{r}-\mathbf{r}')\phi_k(\mathbf{r})\phi_l(\mathbf{r}') \\ t_{ij}^{\text{eff}} &= \int d^3\mathbf{r}\ \phi_i^*(\mathbf{r})\left[\frac{\hat{\mathbf{p}}^2}{2m}+V_p(\mathbf{r};\{\mathbf{R}\})\right]\phi_j(\mathbf{r}). \end{aligned} \tag{2.2}$$

Then, assuming the two-centre integrals vanish for all electrons that are not on the same site, $\epsilon_i = t_{ii}^{\text{eff}}$, or neighbours, $t_i = t_{i,i+1}^{\text{eff}}$, and following the standard semi-empirical practice of neglecting the four-centre integrals (i.e. complete neglect of differential overlap) to only $U_i = V_{iiii}^{\text{eff}}$ and $V_{ij} = V_{ijij}^{\text{eff}}$ we arrive at the PPP Hamiltonian[48],

$$\hat{H}_{PPP} = \sum_{i,\sigma} t_i(\hat{c}_{i+1,\sigma}^\dagger \hat{c}_{i,\sigma} + h.c.) + U\sum_i \left(\hat{N}_{i\uparrow}-\frac{1}{2}\right)\left(\hat{N}_{i\downarrow}-\frac{1}{2}\right) + \frac{1}{2}\sum_{i\neq j} V_{ij}(\hat{N}_i-1)(\hat{N}_j-1), \tag{2.3}$$

where we have set $\epsilon_i = 0$ as this simply defines an arbitrary energy scale and defined $t_i = t_0[1+(-1)^i\delta]$ with δ describing the degree of bond alternation (varying from 0 to 1). We then define the single bond transfer integral, $t_s = t_0(1-\delta)$ and the double bond transfer integral, $t_d = t_0(1+\delta)$. The model Hamiltonian therefore contains Hückel-like neighbouring site-to-site hopping terms described by t_i, an on-site repulsion term, U, representing the energetic penalty of two-electrons occupying the same orbital, and a long-range potential V_{ij}. In practice, the terms in this model are treated as parameters which may be adjusted to account for the approximations made in this derivation.

The long range potential is typically modelled by the semi-empirical Ohno potential, which interpolates between U at short distances and a Coulomb form at long distances,

$$V_r = \frac{U}{\sqrt{1+(\frac{U\epsilon_r r}{14.397})^2}}, \tag{2.4}$$

for distances between sites, r, in Å and energies in eV where ϵ_r is the relative permittivity. We adopt the Chandross-Mazumdar parameterisation (Table 2.1)

U	t_0	ϵ_r	δ	t_s	t_d	r_{C-C}
8.0 eV	2.4 eV	2.0	1/12	2.2 eV	2.6 eV	1.4 Å

Table 2.1: Chandross-Mazumdar PPP parameterisation used in this work.

of the PPP model[49] which has previously been used to investigate carotenoid excited states[37].

2.1.2 Symmetries of Carotenoids

In describing the excited states of carotenoids, we assume an idealised C_{2h} symmetry which holds for systems like lycopene (**7**) but may not be strictly valid for carotenoids with other side-groups and is certainly broken by dynamic fluctuations in solution. Within this point group, excitations can be of A_g or B_u symmetry (determined by their character under inversion) and are additionally described by an emergent symmetry of the PPP Hamiltonian known as particle-hole (PH) parity. In this thesis, we adopt the chemical literature convention in which the ground state, $1^1A_g^-$, is odd-parity by which we mean that the action of an operator $\hat{P}_{PH}$ that swaps the spatial index of an electron and its hole in an exciton gives, $\hat{P}_{PH}\left|1^1A_g^-\right\rangle = -\left|1^1A_g^-\right\rangle$. Dipole-allowed transitions must change both particle-hole symmetry and inversion symmetry and so the bright state in carotenoids is the $1^1B_u^+$ state.

Aggregates introduce additional symmetry elements in the form of rotations which swap chain positions. For vertically-stacked chains, the idealised D_{2h} point group has an additional long-axis C_2 rotation (Fig. 2.1). In the slip-stacked geometry, the system has C_{2h} symmetry although the nature of the C_2 rotation (Fig. 2.1) is different to the single chain case, having the effect of first performing an intrachain inversion followed by a swapping of chains. For clarity, we proceed by describing all states in terms of a single-chain C_{2h} term-symbol in addition to the interchain symmetry element required to fully describe the eigenstate. The character table for the C_{2h} point group is given in Appendix C.

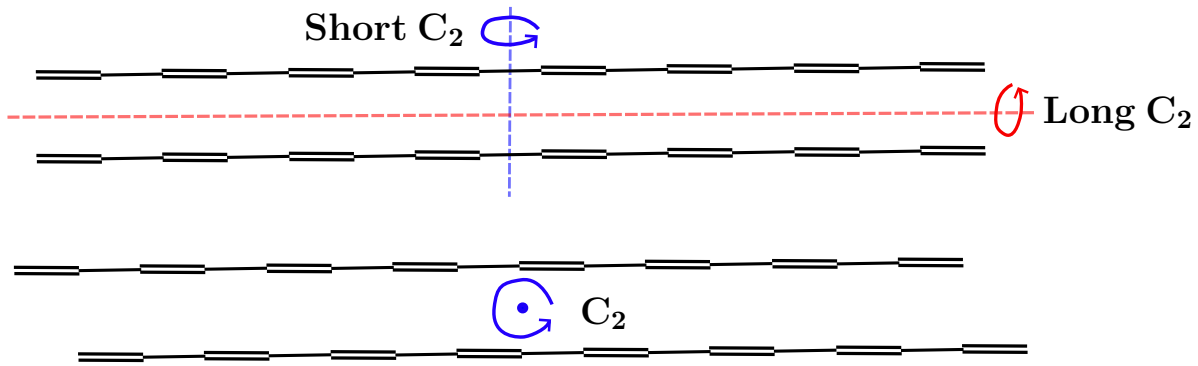


Figure 2.1: Symmetries of ideal linearised carotenoid aggregates in vertically-stacked (D_{2h}) (top) and slip-stacked (C_{2h}) (bottom) geometries.

2.1.3 The Nature of Carotenoid Excited States

Investigations into the excited states of carotenoids with PPP theory have provided a great degree of insight into the nature of the excitations involved. Exciton models provide a real-space quasi-particle description of excited states which can aid in understanding these states, as we now discuss.

The bright $1^1B_u^+$ state is primarily a HOMO $\rightarrow$ LUMO transition that is described as a Frenkel exciton — a bound electron-hole pair that is delocalised across the whole π-system[48]. It is also considered to have some Wannier character, referring to a contribution to the wavefunction of charge-transfer configurations with larger electron-hole separation[50].

The key point of interest in polyenes is that the $1^1B_u^+$ state is not the lowest lying singlet excited state. Instead, there are dark states, such as $2^1A_g^-$, which are invisible to absorption spectroscopy due to their doubly excited nature. Light absorption, which is an inherently one-photon-one-electron process, is unable to populate these states. Instead, they are accessed by rapid internal conversion from the bright state and act to suppress fluorescence.

The dark $2^1A_g^-$ state in polyenes was first described in the early 1970s[51] and was found to require multiple configuration interaction in theoretical calculations to agree with experimental energies[52–55]. Tavan and Schulten first described

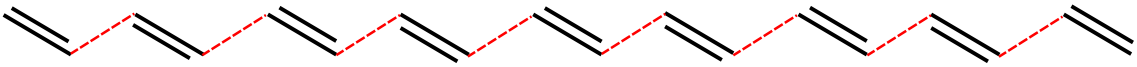


Figure 2.2: The molecular exciton picture of conjugated polymers. In this view, a polyene is essentially a J-aggregate of ethylenes.

this state as a triplet-pair, meaning that the electronic structure behaves as if two triplets were confined to one polymer but coupled together so as to become an overall singlet excitation[56]. Further research has uncovered a larger family of triplet-pair states ($2^1A_g^-, 1^1B_u^-, 3^1A_g^-, ...$) that consist of the same fundamental excitation but are characterised by different pseudomomentum quantum numbers[37].

2.2 The Model Hamiltonian and Basis

2.2.1 Single-chain Hamiltonian

The molecular exciton approach, first described by Simpson[57], treats excitations in a conjugated polymer as being built from excitations within the monomers. The polymer linkage is then treated as a perturbation onto the set of independent simple monomer excitations as shown in Figure 2.2.

In this framework, the polyene excited states are expressed as direct products of ethylene monomer states. The ethylene eigenstates and their energies are derived exactly from the PPP Hamiltonian in Appendix A and shown in the atomic orbital representation in Figure 2.3. An exact calculation could be made using the ethylene basis states rather than atomic orbitals[58, 59] but is limited to small systems ($<$ 5 ethylene units). One method to circumvent this problem is to select the most important electronic configurations relevant to the low-energy states of interest in singlet fission processes[60]. This approach, considering relatively few excitations, was shown to give good results, even at low values of δ where the assumptions of the dimerised model should break down[61]. In this thesis, we adopt a reduced basis model first investigated for strongly dimerised systems[62] and later shown to give a qualitative description of the triplet-pair states in polyenes with small δ[63].

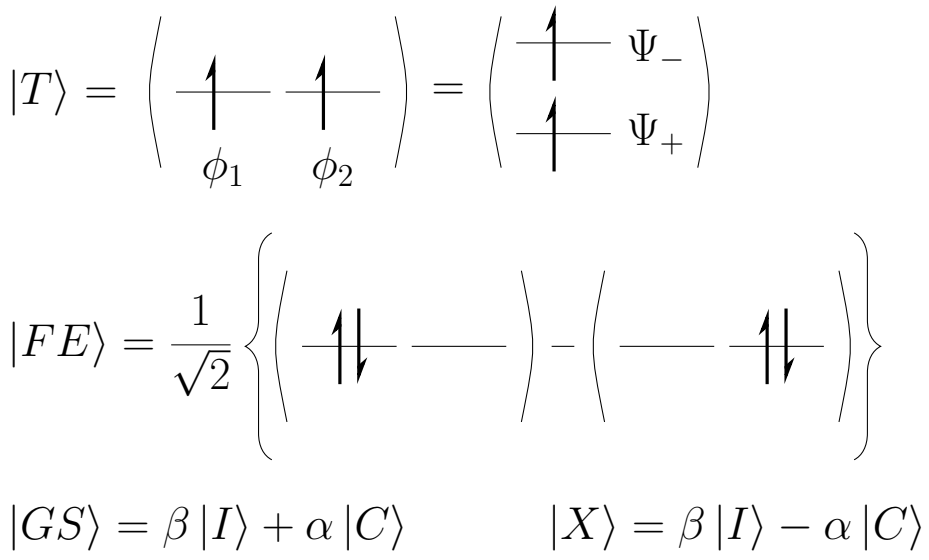


Figure 2.3: The four eigenstates of ethylene in the PPP Hamiltonian. The basis states $|I\rangle$ and $|C\rangle$ are defined in Fig. 2.4. Correspondence between atomic orbitals, ϕ_i and molecular orbitals, Ψ_i, is shown.

To construct this minimal model, we restrict our choice of electronic configurations to those that have been shown to be the dominant contributors to the full CI wavefunctions[59]. For the ground state, this is simply,

$$|GS\rangle = \bigotimes_i |GS_i\rangle\,, \tag{2.5}$$

where the product is over all ethylene units. This ground state has intramonomer correlation but lacks any intermonomer correlation. We do not explicitly include this ground state in our basis but define all excitations as relative to the $|GS\rangle$ vacuum. The simplest excitations are equivalent to one-monomer excited states, the lowest being the odd PH-symmetry triplet,

$$|T, M_s; j\rangle = |T_j, M_s\rangle \bigotimes_{i\neq j} |GS_i\rangle\,, \quad \hat{P}_{PH}\,|T, M_s; j\rangle = -\,|T, M_s; j\rangle\,, \tag{2.6}$$

where M_s is the spin magnetic quantum number (1, 0, or -1) and $E_T = V_1 - E_{GS}$ where V_l is the Ohno potential (Eq. 2.4) between carbon atons with a separation of l bonds. This is followed by the even PH-symmetry singlet excitation,

$$|FE; j\rangle = |FE_j\rangle \bigotimes_{i\neq j} |GS_i\rangle\,, \quad \hat{P}_{PH}\,|FE; j\rangle = +\,|FE; j\rangle\,, \tag{2.7}$$

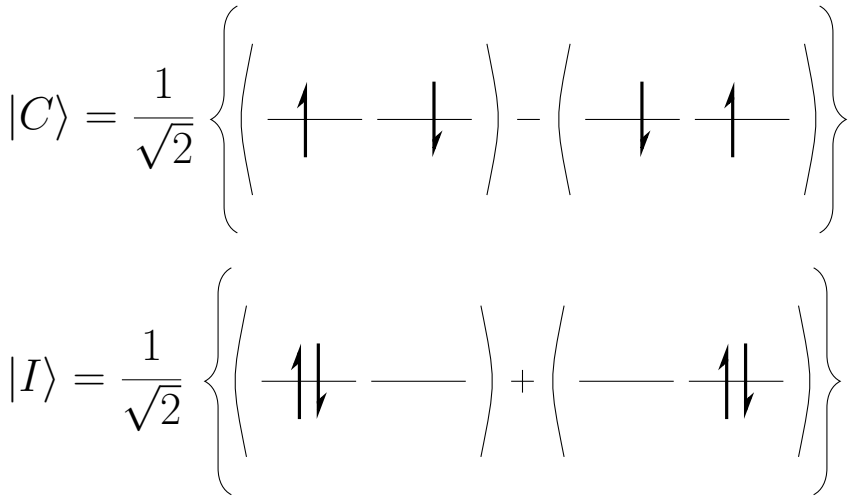


Figure 2.4: Covalent, $|C\rangle$, and ionic, $|I\rangle$, basis states for ethylene.

with $E_{FE} = U - E_{GS}$, where we denote the singlet ethylene monomer excitation as a Frenkel exciton basis state as it consists of an electron-hole pair with minimal spatial separation.

To describe the ability of these excitons to delocalise across the system, we consider the intrachain charge-transfer exciton with separated electron ($|e^-; i\rangle$) and hole ($|h^+; j\rangle$),

$$|EX_1; i, j\rangle = \left|e^-; i\right\rangle \left|h^+; j\right\rangle \bigotimes_{k\neq i,j} |GS_k\rangle\,, \tag{2.8}$$

where with $i > j$ and its particle-hole swapped counterpart $\hat{P}_{PH}\,|EX_1; i, j\rangle = |EX_1; j, i\rangle = -\,|EX_2; i, j\rangle$ (defined in the MO representation for the singlet case in Fig. 2.5) with

$$E_{EX}(j-i) = U + 2V_1 - 2t_d - 2E_{GS} - \tilde{V}_{|j-i|}, \tag{2.9}$$

where the electron-hole Coulomb attraction is

$$\tilde{V}_l = (V_{2l-1} + 2V_{2l} + V_{2l+1})/4. \tag{2.10}$$

For our PPP parameters, we find $E_{EX}(1)$ proximal in energy to E_{FE} and so we explicitly include the singlet charge-transfer basis state and find that it couples with

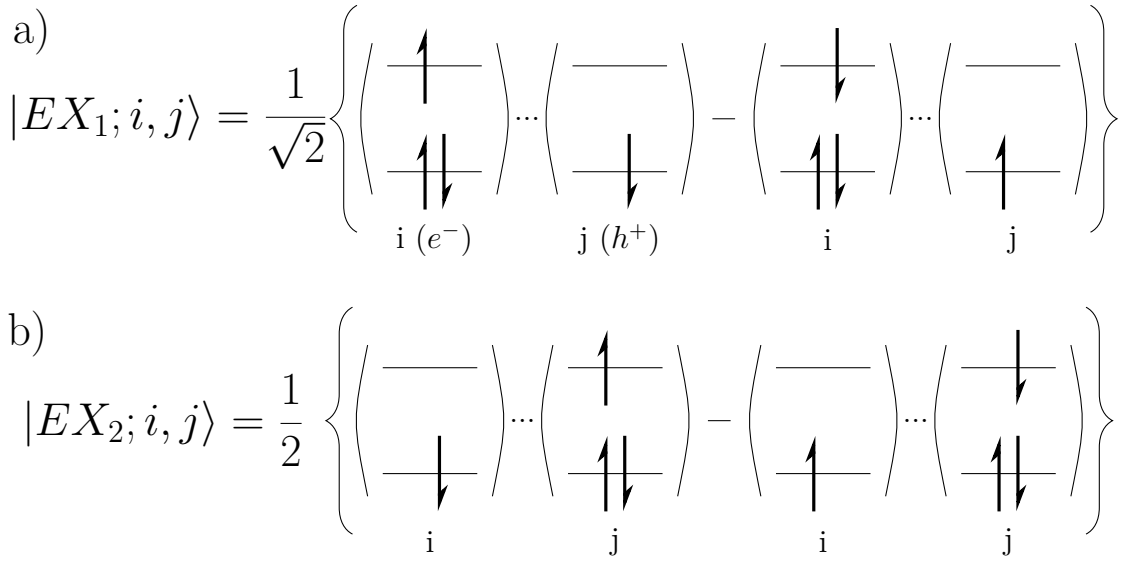


Figure 2.5: Molecular orbital representation of the singlet charge-transfer states $\left|EX_{1(2)}\right\rangle$.

the FE basis state by an electron-transfer across a single bond,

$$V_{EX_{1(2)}-FE} = \langle EX_{1(2)};i,i+1|\hat{H}|FE;i\rangle = +(-)\frac{(\alpha+\beta)t_s}{\sqrt{8}}, \tag{2.11}$$

and see that only the positive PH-symmetrised EX basis states, $|EX^+\rangle = 1/\sqrt{2}(|EX_1\rangle - |EX_2\rangle)$ couple to FE basis states. The EX states are able to hop across monomer units with transfer integral,

$$t_{EX} = \left\langle EX_{1(2)};i+1,j\right| \hat{H} \left|EX_{1(2)};i,j\right\rangle = \frac{(\alpha+\beta)^2 t_s}{4}, \tag{2.12}$$

which, through V_{EX-FE}, allows the FE basis states to delocalise across the system. Additionally, we include the transition dipole-transition dipole coupling term,

$$J_{FE}^{\text{intra}} = \langle FE;i\pm 1|\,\hat{H}\,|FE;i\rangle = -\beta^2(V_1 - 2V_2 + V_3), \tag{2.13}$$

which describes the Coulomb-induced Förster resonance energy transfer of FE excitations between ethylene monomer units.

For the triplet states, however, we find a large energy separation between $|T\rangle$ and triplet $|EX\rangle$ excitations (~4 eV) and so treat triplet hopping through a superexchange mechanism (derived in Appendix B),

$$t_T^{\text{intra}} = \langle T;i\pm 1|\,\hat{H}\,|T;i\rangle = -\frac{\alpha^2 t_s^2}{E_{EX}^{NN} - E_T}, \tag{2.14}$$

where α^2 is the weight of the covalent basis state, $|C\rangle$ (Fig. 2.4), in the ethylene ground state and E_{EX}^{NN} is the energy of the nearest-neighbour singlet charge-transfer exciton.

The intrachain singlet triplet-pair excitation can then be defined as

$$|iTT;i,j\rangle = \frac{1}{\sqrt{3}}(|T,1;i\rangle\,|T,-1;j\rangle - |T,0;i\rangle\,|T,0;j\rangle + |T,-1;i\rangle\,|T,1;j\rangle), \quad (2.15)$$

where the triplet excitations act as hard-core bosons forbidden from occupying the same site. The final interaction to consider is the coupling between triplet-pair and charge-transfer basis states which facilitates the binding of the triplet-pair,

$$V_{EX-iTT} = \langle iTT;i,i\pm1|\,\hat{H}\,|EX_{1,2};i,i\pm1\rangle = -\sqrt{\frac{3}{8}}t_s, \quad (2.16)$$

so that iTT couples only with $|EX^-\rangle = 1/\sqrt{2}(|EX_1\rangle + |EX_2\rangle)$. Barford showed that this interaction represents the principal mechanism by which the triplet-pairs in the $2^1A_g^-$ family of states are bound[63]. The binding energy (the gap between the singlet triplet-pair states and the unbound quintet triplet-pair states) has contributions from two effects. Firstly, the hybridisation of the triplet-pair and charge-transfer bands results in the lowering of the energy of the first members of the resultant $2^1A_g^-$-like band. Secondly, the rapid fall of the electron-hole Coulomb attraction, $\tilde{V}_l$, with increasing separation lends energetic stability to iTT states made up of proximal triplet excitations.

The particular basis that we consider was first used to describe the $\delta \to 1$ limit[62, 64], where the polymer most closely resembles a dimerised ethylene chain, but has been shown to also provide a good physical description even for much smaller, more realistic values of δ[63]. Despite its simplicity, our model does not display the size-inconsistency problems common to low-excitation configuration interaction calculations (single or double) where certain eigenstates (commonly, the ground state) are significantly more sensitive to system size than others. This success is due to the implicit inclusion of N-tuply excited configurations inside of the ground

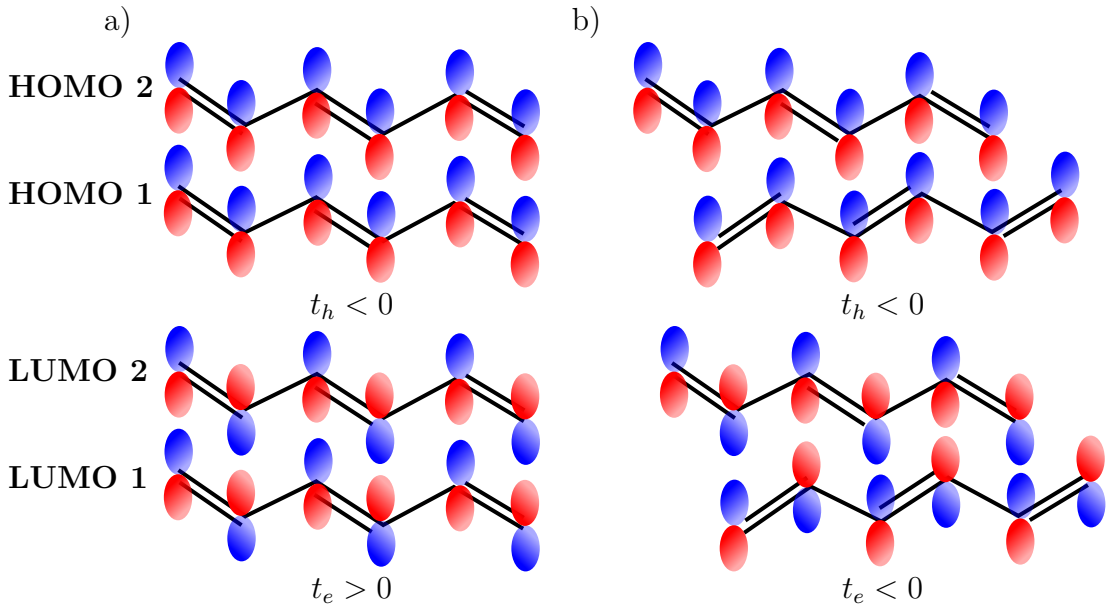


Figure 2.6: HOMO and LUMO overlap of ethylene units within chains and resulting electron, $t_e = \langle LUMO_1 | \hat{H} | LUMO_2 \rangle$, and hole, $t_h = -\langle HOMO_1 | \hat{H} | HOMO_2 \rangle$, transfer integrals for a) vertically-stacked and b) slip-stacked ethylene units.

state[50, 60]. In principle, we should also include the EX/GS coupling which would allow for a description of intermonomer correlation but this step introduces a vast expansion of the basis (as each basis state would have many potential charge-transfer configurations in the vacuum surrounding the excitation) and the large energy gap suggests that this process can be neglected.

In summary, the intrachain singlet Hamiltonian is written as

$$\hat{H}_{\text{intra}} = \hat{H}_{iTT} + \hat{H}_{FE} + \hat{H}_{EX} + \hat{V}_{EX-iTT} + \hat{V}_{EX-FE}, \tag{2.17}$$

with $\hat{H}_X$ encoding the energy and hopping terms of basis state X while $\hat{V}_{X-Y}$ describes the hybridisation of basis states X and Y.

2.2.2 Aggregate Hamiltonian

In the decoupled limit, aggregate states may be expressed exactly as products of single-chain eigenstates. We then introduce an interchain hopping term, t_p, perpendicular to t_s, which allows excitations to delocalise across the aggregate. We model the aggregate by considering σ-type overlap of neighbouring polymer

π-systems (Fig. 2.6) where t_p (in eV) is found from the Mulliken formula[65, 66],

$$t_p(D) = 10.6 \times \exp(-D\xi)\left(\frac{1}{15}(D\xi)^4 + \frac{2}{15}(D\xi)^3 - \frac{1}{5}(D\xi)^2 - D\xi - 1\right), \quad (2.18)$$

where $\xi = 3.07$ Å^{-1} and D is the interchain separation in Å.

There are two new types of basis state that are required to describe the aggregate structure. The first is the interchain singlet charge-transfer state between index i on chain x and j on chain $\bar{x}$ where $\bar{x} < x$,

$$|CT_1; i_x, j_{\bar{x}}\rangle = \left|e^-; i_x\right\rangle \left|h^+; j_{\bar{x}}\right\rangle \bigotimes_{k,x\neq i(x),j(\bar{x})} |GS_{k_x}\rangle\,, \quad (2.19)$$

and its inverted electron-hole counterpart $\hat{P}_{PH}\,|CT_1; i_x, j_{\bar{x}}\rangle = |CT_1; j_x, i_{\bar{x}}\rangle = -\,|CT_2; i_x, j_{\bar{x}}\rangle$. These allow for hopping of excitons across chains where $E_{CT}(i_x, j_{\bar{x}})$ is similar to E_{EX} except $\tilde{V}$ extends across chains as,

$$\tilde{V}_l = (V_{\|D,2l-1\|} + 2V_{\|D,2l\|} + V_{\|D,2l+1\|})/4, \quad (2.20)$$

and the electron and hole of a CT basis state are allowed to hop along their respective chains (in analogy to EX) with transfer integral, t_{EX}. The second new basis state is the interchain singlet triplet-pair in which each chain has a single triplet excitation,

$$\begin{aligned} |TT; i_x, j_{\bar{x}}\rangle = \frac{1}{\sqrt{3}}\Big(&|T, 1; i_x\rangle\,|T, -1; j_{\bar{x}}\rangle \\ &- |T, 0; i_x\rangle\,|T, 0; j_{\bar{x}}\rangle \\ &+ |T, -1; i_x\rangle\,|T, 1; j_{\bar{x}}\rangle\Big), \end{aligned} \quad (2.21)$$

where $|T; i_x\rangle$ is a triplet excitation on site i of chain x and $E_{TT} = 2E_T$.

2.2.2.1 Vertically Stacked Dimer

We first consider the simplest case of the carotenoid dimer with vertical stacking (Fig. 2.6a) where EX states only couple to CT states with the same intrachain indices but on neighbouring chains,

$$\begin{aligned} \text{Hop up: } V_{EX-CT} &= \langle CT_{1,2}; i_2, j_1|\,\hat{H}\left|EX_{1(2)}; i_1, j_1\right\rangle = -(+)\frac{(\alpha+\beta)^2 t_p}{2}, \\ \text{Hop down: } V_{EX-CT} &= \langle CT_{1,2}; i_2, j_1|\,\hat{H}\left|EX_{1(2)}; i_2, j_2\right\rangle = +(-)\frac{(\alpha+\beta)^2 t_p}{2}. \end{aligned} \quad (2.22)$$

FE basis states are coupled to CT states which enables a second-order hopping process across chains,

$$V_{FE-CT} = \left\langle FE; i_{2(1)} \right| \hat{H} \left| CT_{1,2}; i_2, i_1 \right\rangle = +(-)\frac{(\alpha+\beta)t_p}{\sqrt{2}}, \tag{2.23}$$

where we only consider the nearest-neighbour hopping so that monomer indices remain the same. As expected, the coupling remains only for the positive PH-symmetry CT combination, $|CT^+\rangle = 1/\sqrt{2}(|CT_1\rangle - |CT_2\rangle)$. FE basis states can also move directly via the interchain transition-dipole transition-dipole coupling term,

$$J_{FE}^{\text{inter}} = \langle FE; i, x \pm 1| \hat{H} |FE; i, x\rangle = 2\beta^2(V_D - V_{\|D,1\|}). \tag{2.24}$$

We additionally allow for interchain superexchange triplet hopping via virtual interchain triplet charge-transfer excitations,

$$t_T^{\text{inter}} = \langle iTT; i, x, j, x| \hat{H} |TT; i, x, j, x \pm 1\rangle = -\frac{2t_p^2}{E_{CT}^{NN} - E_T}, \tag{2.25}$$

when $i \neq j$.

The resulting eigenstates can be described as mixtures of uncoupled ($t_p = 0$) intra and interchain eigenstates. We first investigate the long-axis combinations of Frenkel exciton basis states,

$$\left|FE^{\pm}; i\right\rangle = \frac{1}{\sqrt{2}}\Big(|FE; i, 1\rangle \pm |FE; i, 2\rangle \Big). \tag{2.26}$$

These states are split symmetrically from the single-chain barycentre by the dipolar interaction (Eq. 2.24) as in Fig. 1.4 with $|FE^+\rangle$ being the higher energy dipole-allowed bright state and $|FE^-\rangle$ the lower energy optically inaccessible dark state. We also see that the FE-CT interaction (Eq. 2.23) is non-zero only for $|FE^-\rangle$, so that the dark state is further pushed down in energy beyond the dipole splitting gap (Fig. 2.7a). The bright state is still able to gain CT character, although this is through a much weaker second-order interaction mediated by EX.

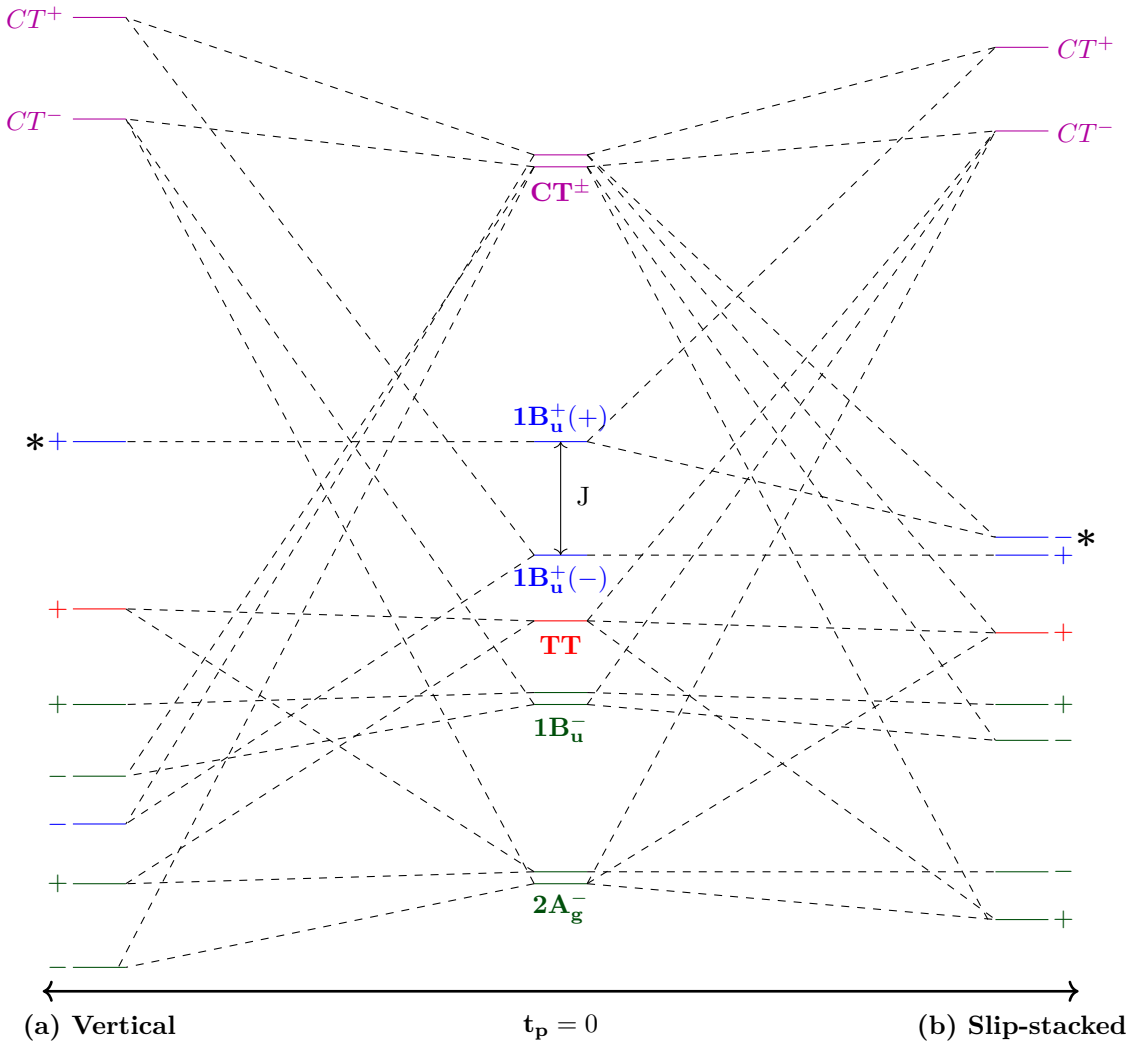


Figure 2.7: Schematic MO diagram change upon increasing t_p in aggregates in a) vertically and b) slip-stacked geometries. J indicates the H-aggregate transition dipole-transition dipole splitting. $CT^\pm$ represent the manifold of high-energy charge-transfer states while TT is the lowest energy singlet interchain triplet-pair state. Single-chain term symbols are used in addition to $(+)/(-)$ which denote the a) long-axis symmetry or b) overall C_2 symmetry. * denotes the bright state in each geometry.

Similarly, the EX-CT coupling (Eq. 2.22) is non-zero only for the long-axis anti-symmetric combination of intrachain states, so that both the FE and iTT intrachain anti-symmetric combinations are lowered further in energy. In contrast, the iTT-TT coupling (Eq. 2.25) is present only for long-axis symmetric intrachain triplet-pair states which would lower the iTT(+) states, however (as shown in Fig. 2.7) the smaller magnitude of the interchain superexchange coupling makes this effect marginal for realistic coupling regimes.

2.2.2.2 Slip-stacked Dimer

Slipping one chain by one bond introduces the additional complexity that one ethylene unit on one chain now has direct orbital overlap with two distinct ethylene units on the other chain, where the sign of the transfer integrals are changed from the vertically stacked case (Fig. 2.6b). The PPP Hamiltonian therefore still allows hops from the same dimer index on one chain to another chain, but additionally allows $i \to i-1$ downward (from chain 2 to 1) hops and $i \to i+1$ upwards (from chain 1 to 2) hops. Hence, the EX-CT coupling takes the more complicated structure

$$\begin{aligned} \text{Hop up: } \hat{H}\,|EX_a; i_1, j_1\rangle &= s_{ab}\frac{|V_{EX-CT}|}{2}\Big[\,|CT_b; i_2/(i+1)_2, j_1\rangle + \\ &\qquad |CT_b; j_2/(j+1)_2, i_1\rangle\,\Big], \\ \text{Hop down: } \hat{H}\,|EX_a; i_2, j_2\rangle &= s_{ab}\frac{|V_{EX-CT}|}{2}\Big[\,|CT_b; i_2, j_1/(j-1)_1\rangle + \\ &\qquad |CT_b; j_2, i_1/(i-1)_1\rangle\,\Big], \end{aligned} \tag{2.27}$$

where $s_{ab} = 1$ if $a = b$ and -1 if $a \neq b$. The FE-FE dipolar coupling is reduced relative to vertical stacking,

$$\langle FE; i_2/(i+1)_2|\,\hat{H}\,|FE; i_1\rangle = \beta^2(2V_{\|D,1\|} - V_D - V_{\|D,2\|}), \tag{2.28}$$

and the FE-CT coupling takes the form

$$\langle FE; i_2|\,\hat{H}\,|CT_b; i_2, i_1/(i-1)_1\rangle = \langle FE; i_1|\,\hat{H}\,|CT_b; i_2/(i+1)_2, i_1\rangle = (-1)^b\frac{|V_{FE-CT}|}{2}, \tag{2.29}$$

where the first matrix element corresponds to hopping down and the second hopping up. Triplet-hopping retains the same phase, but has a reduction in magnitude between each ethylene unit,

$$\langle T; i_2/(i+1)_2|\,\hat{H}\,|T; i_1\rangle = \frac{\alpha^2}{2}t_T^{\text{inter}}. \tag{2.30}$$

The only new interaction that is present in this geometry is a direct coupling between interchain triplet-pair states and charge-transfer states,

$$\langle CT_{1,2}; i_2, i(-1)_1|\,\hat{H}\,|TT; i_2, i(-1)_1\rangle = +(-)\sqrt{\frac{3}{8}}t_p. \tag{2.31}$$

Site	1	2	3	4	5	6	7	8	9	10	11
ϵ_i/**eV**	-2.15	-0.60	1.81	1.44	-2.31	-0.76	1.28	1.15	-2.60	-1.00	1.01

Table 2.2: On-site energy shifts due to lycopene methyl substitution. The other half of the chain has reflected values.

The relationship to the vertical-stacked case can be understood as a halving of the electron-transfer channel between each ethylene unit (which multiplies in the superexchange hop to give a factor of $2/\alpha^2 \approx 3$). The MO diagram (Fig. 2.7) is thus similar to the vertical case but with smaller splittings and phase changes in the transfer integrals resulting in the bright FE combination (C_2 anti-symmetric) now coupling to the charge-transfer manifold.

The aggregate Hamiltonian may then be written as

$$\hat{H}_{inter} = \hat{H}_{TT} + \hat{H}_{CT} + \hat{J}_{FE}^{\text{inter}} + \hat{t}_{T}^{\text{inter}} + \hat{V}_{EX-CT} + \hat{V}_{FE-CT}\ (+\hat{V}_{TT-CT}), \qquad (2.32)$$

where the final term appears only in the slip-stacked geometry. The diabatic (pure symmetry) Hamiltonian is constructed in the local ethylene exciton-basis as

$$\hat{H}_{\text{diab}}^{\text{Eth}} = \hat{H}_{\text{intra}} + \hat{H}_{\text{inter}}, \qquad (2.33)$$

which is diagonalised by S_{diab} to give the diabatic eigenbasis $H_{\text{diab}}^{\text{eig}} = S_{\text{diab}}^{-1}\hat{H}_{\text{diab}}^{\text{Eth}}S_{\text{diab}}$.

2.2.3 Symmetry Breaking

In order to simulate real processes, we require a method for allowing conversion between the pure symmetry eigenstates (diabatic states) we have discussed so far. The most important symmetry to break is the PH symmetry, which prevents the bright $1^1B_u^+$ state from coupling to the negative PH symmetry triplet-pair states. We therefore add a symmetry-breaking term to the Hamiltonian,

$$\hat{H}_{\epsilon} = \sum_i \epsilon_i(\hat{N}_i - 1), \qquad (2.34)$$

which describes the effects of the substituents on the polyene. Electrons therefore experience a ϵ_i shift while holes feel a $-\epsilon_i$ shift, which makes $|EX_1\rangle$ and $|EX_2\rangle$

(and like CT states) non-equivalent, allowing for mixing of diabatic states to form symmetry-broken eigenstates (adiabatic states). Tim Georges, following the method of Manawadu et al.[67], performed a DFT calculation on lycopene (**7**) with the B3LYP functional and the def2-TZVP basis set to find the values given in Table 2.2.

Additionally, real aggregates do not display perfect C_{2h} symmetry due to structural disorder where one part of the chains may be closer together than another part. We simulate this by using a random Gaussian noise with a mean of D and a standard deviation, σ_d, to determine the distance between every nearest-neighbour pair of interchain carbon atoms. We then use the Mulliken formula (Eq. 2.18) to find the value of t_p that should be used for the hopping terms. This term has the effect of breaking intrachain inversion symmetry, allowing for the mixing of B_u and A_g intrachain states. The adiabatic Hamiltonian is thus constructed as

$$\hat{H}^{\text{Eth}}_{\text{adiab}} = \hat{H}_{\text{intra}} + \hat{H}_{\text{inter}}(t_p; \sigma_d) + \eta\hat{H}_{\epsilon}, \tag{2.35}$$

where η controls the degree of PH-breaking and σ_d controls the degree of intrachain symmetry-breaking.

2.2.4 Vibronic Coupling

It has been found that nonadiabatic effects are important in carotenoids[68, 69]. As our model has no explicit vibrational modes, we consider intrachain vibronic coupling by forming the intrachain equivalent Hamiltonian,

$$\hat{H}_{\text{1-chain}} = \hat{H}_{\text{intra}} + \hat{H}_{\text{inter}}(J^{\text{inter}} = 0, t_p = 0), \tag{2.36}$$

which spans the full aggregate basis but consists of uncoupled chains and is diagonalised by $S_{\text{1-chain}}$. We rotate $\hat{H}^{\text{Eth}}_{\text{adiab}}$ into the intrachain basis with the transformation, $\hat{H}^{\text{1-chain}}_{\text{adiab}} = S^{-1}_{\text{1-chain}}\hat{H}^{\text{Eth}}_{\text{adiab}}S_{\text{1-chain}}$ and then include vibronic coupling-driven conversion by introducing an off-diagonal between the $1^1B_u^-$ and $2^1A_g^-$ one-chain

equivalent states,

$$\left\langle 1^1B_u^- \right| \hat{H}_{VC} \left| 2^1A_g^- \right\rangle = \lambda, \tag{2.37}$$

where λ was found by summing the lycopene interstate linear vibronic coupling parameters of anti-symmetric modes, giving $\lambda = 0.205$ eV[69]. In principle, this should be applied between any set of eigenstates, but we find this term to be the most important due to its role in breaking intrachain inversion symmetry.

Finally, we rotate the vibronically-coupled Hamiltonian back into the ethylene basis, $\hat{H}_{VC}^{\text{Eth}} = S_{\text{1-chain}} \hat{H}_{VC}^{\text{1-chain}} S_{\text{1-chain}}^{-1}$, and diagonalise to obtain the symmetry-broken eigenstates, $\hat{H}_{\text{adiab}}^{\text{eig}} = S_{\text{adiab}}^{-1} \hat{H}_{\text{adiab}}^{\text{Eth}} S_{\text{adiab}}$.

2.3 Time Evolution

2.3.1 Liouville-von Neumann Equation

The unitary evolution of a pure quantum-mechanical state vector, $|\Psi\rangle$, is described by the time-dependent Schrödinger equation,

$$i\hbar \frac{\partial |\Psi(t)\rangle}{\partial t} = \hat{H} |\Psi(t)\rangle. \tag{2.38}$$

A generalisation of this equation is found by introducing the density operator,

$$\hat{\rho} = \sum_i p_i |\Psi_i\rangle\langle\Psi_i|, \tag{2.39}$$

where the sum is over an ensemble of states of the system, $|\Psi_i\rangle$, with associated probability of being in the state, p_i.

Following the differentiation of (2.39) and the insertion of (2.38), we arrive at the Liouville-von Neumann equation for the time-evolution of the density operator,

$$\frac{\partial \hat{\rho}}{\partial t} = -\frac{i}{\hbar}[\hat{H}, \hat{\rho}]. \tag{2.40}$$

2.3.2 The Redfield Equation

The density operator's utility becomes evident when describing the dynamics of a real molecular system coupled to a surrounding environment which acts as a heat bath. This situation is described by the Redfield equation,

$$\frac{\partial \hat{\rho}_S(t)}{\partial t} = -\frac{i}{\hbar}[\hat{H}_S, \hat{\rho}_S(t)] + \hat{\hat{R}}\hat{\rho}_S(t), \tag{2.41}$$

where the first term on the right describes unitary dynamics of the system under the quantum Liouville equation and the second describes the dissipative effects of the bath on the system. As shown in Appendix D, this equation arises from assuming weak system-bath coupling as well as neglecting memory effects on bath dynamics.

Upon making the secular approximation (Appendix D.0.2), the time evolution of the populations (diagonals of ρ_S) and coherences (off-diagonals of ρ_S) are decoupled and take the form,

$$\begin{aligned} \frac{\partial P_a(t)}{\partial t} &= \sum_c P_c(t) k_{c\to a} - P_a(t)\mathcal{K}_a, \\ \frac{\partial \rho_{ab}}{\partial t} &= -\left(i\omega_{ab} + \frac{1}{2}(\mathcal{K}_a + \mathcal{K}_b)\right)\rho_{ab}. \end{aligned} \tag{2.42}$$

where $k_{c\to a}$ is the rate of population transfer from state c to state a and $\mathcal{K}_a = \sum_i k_{a\to i}$.

Berkelbech et al.[70] showed that the secular Redfield equation approach is appropriate for modelling singlet fission processes and found that the form of the spectral density had little effect on the dynamics. Our calculations are performed at $T = 300$ K and we choose the Drude-Lorentz spectral density,

$$J(\omega) = 2\lambda \frac{\omega\omega_0}{\omega^2 + \omega_0^2}, \tag{2.43}$$

where $\omega_0 = 0.2$ eV is the Debye cut-off frequency and $\lambda = 50$ meV is the bath reorganisation energy which we assume to be the same for all eigenstates.

3
Computational Methods

3.1 Density Matrix Renormalisation Group

The Density Matrix Renormalisation Group (DMRG) is a Hilbert space truncation procedure[71, 72] that allows for systematic reduction in computational complexity with accuracy up to an arbitrary truncation error. In DMRG, the polyene is constructed as a lattice of sites which is partitioned into system and environment blocks which make up the overall superblock. The algorithm can be described as follows:

1. Exactly solve the Hamiltonian for a small chain (e.g. 2 sites per block).

2. Augment each block with a new site (Fig. 3.1), construct the new Hamiltonian and diagonalise to obtain the superblock ground state and targeted excited state wavefunctions, $|\Psi_n\rangle$.

3. Find the system reduced density matrix by tracing over the environment in the superblock density matrix, $\rho_S = Tr_E(\sum_n \kappa_n |\Psi_n\rangle \langle\Psi_n|)$ where κ_i describes the weight of the targeted states in the superblock density matrix (usually taken to be equal, $\sum_i \kappa_i = 1$).

4. Diagonalise ρ_S and keep the eigenvectors with the top k largest eigenvalues as the new truncated basis.

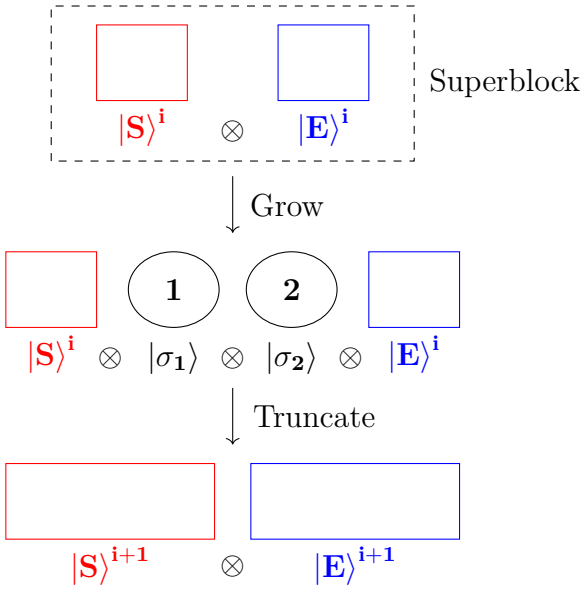


Figure 3.1: Schematic of a DMRG iteration. The chain is partitioned into system (S) and environment (E) blocks which are augmented by new sites 1 and 2 respectively.

5. Rotate operators into this truncated basis and repeat from (2) until system has grown to the desired size.

DMRG is particularly effective for solving one-dimensional problems due to the exponential decay of the eigenvalues of the reduced density matrix with system size[73]. This has led to its widespread application in the study of polyene electronic structure[74, 75], but makes it unsuitable for the investigation of large two- and three-dimensional aggregate systems.

3.2 Short Iterative Arnoldi Propagator

The differential equation for the time-evolution of the coherences, $\hat{\rho}_{\alpha\beta}$, according to the secular Redfield equation (Eq. D.17) can be integrated exactly to,

$$\hat{\rho}_{\alpha\beta} = \hat{\rho}_{\alpha\beta}(0)\ \exp(-i\omega_{\alpha\beta} - \frac{1}{2}(\mathcal{K}_a + \mathcal{K}_b))t, \tag{3.1}$$

but the populations evolve according to a more complicated coupled differential equation which can be cast into the matrix form,

$$\frac{\partial}{\partial t}\mathbf{P}(t) = \mathbf{K}\mathbf{P}(t), \tag{3.2}$$

where $\mathbf{P}(t)$ is the vector of populations and $\mathbf{K}$ is a matrix formed from the rate constants, $\mathbf{K}_{ab} = k_{b\to a} - \delta_{ab}\sum_i k_{a\to i}$. If $\mathbf{K}$ is diagonalisable, we find the exact solution,

$$\mathbf{P}(t) = \exp(\mathbf{K}t)\mathbf{P}(0) = \mathbf{L}\exp(\mathbf{\Lambda}t)\mathbf{L}^{-1}\mathbf{P}(0), \tag{3.3}$$

where $\mathbf{L}$ is the matrix of eigenvectors of $\mathbf{K}$ with corresponding eigenvalues $\mathbf{\Lambda}$. However, the $\mathbf{L}$ considered in this work was found to be ill-conditioned making inversion routines numerically unstable.

To avoid this direct inversion, we use the short iterative Arnoldi propagator[76] which is a generalisation of the short iterative Lanczos propagator[69] to non-hermitian matrices such as $\mathbf{K}$. The full matrix $\mathbf{K}$ is reduced to an m-dimensional Krylov space ($\mathcal{K}_m$) built from vectors constructed by repeated applications of $\mathbf{K}$ to $\mathbf{P}$ with each new vector being orthogonalised to give $\mathbf{v_m}$,

$$\mathcal{K}_m(\mathbf{K},\mathbf{P}) = \mathrm{span}\{\mathbf{P},\mathbf{KP},\mathbf{K^2P},...,\mathbf{K^{m-1}P}\} = \mathrm{span}\{\mathbf{v_1},\mathbf{v_2},\mathbf{v_3},...,\mathbf{v_{m-1}}\}. \tag{3.4}$$

The representation of $\mathbf{K}$ in Krylov space takes the upper Hessenberg form,

$$\mathbf{k} \approx \mathbf{v}^\dagger\mathbf{K}\mathbf{v}, \tag{3.5}$$

where $\mathbf{v}$ is the transformation matrix built out of the orthonormal vectors $\mathbf{v_m}$. The matrix $\mathbf{k}$ is diagonalised by $\mathbf{l}$ to give the eigenvalues $\boldsymbol{\lambda}$ which allows us to construct the approximate propagator,

$$\exp(\mathbf{K}t) \approx \mathbf{v}\mathbf{l}\exp(\boldsymbol{\lambda}t)\mathbf{l}^{-1}\mathbf{v}^\dagger. \tag{3.6}$$

The result is exact for $m = \dim(\mathcal{H})$ but the method converges rapidly and, in practice, a much smaller value ($m = 20$) can be used to get good results.

In our dynamics calculations, we choose the initial state to be the delocalised bright Frenkel exciton, which is found by selecting the lowest dipole-allowed diabatic (pure symmetry) eigenstate, so that the initial density operator is

$$\boldsymbol{\rho}_{\mathrm{diab}}(0) = \left|1^1B_u^+\right\rangle\left\langle 1^1B_u^+\right|. \tag{3.7}$$

It is important to note that the bright state is the +ve long-axis C_2 symmetry $1^1B_u^+$ state for vertically-stacked chains, and the −ve C_2 symmetry $1^1B_u^+$ state for slip-stacked chains.

The density matrix is propagated in the adiabatic Hamiltonian eigenbasis, so we consecutively rotate into the ethylene exciton basis and then the diagonal adiabatic basis,

$$\boldsymbol{\rho}_{\text{eig}}(0) = \mathbf{S}_{\text{adiab}}^{-1}\mathbf{S}_{\text{diab}}\boldsymbol{\rho}_{\text{diab}}(0)\mathbf{S}_{\text{diab}}^{-1}\mathbf{S}_{\text{adiab}}. \tag{3.8}$$

At each time-step in propagation, we rotate into the ethylene exciton basis and sum the population of each kind of basis state (FE, iTT, EX, TT, CT) from the diagonal of $\boldsymbol{\rho}_{\text{Eth}}(t) = \mathbf{S}_{\text{adiab}}\boldsymbol{\rho}_{\text{eig}}(t)\mathbf{S}_{\text{adiab}}^{-1}$. Additionally, we collect the main contributing diabatic states from $\boldsymbol{\rho}_{\text{diab}}(t) = \mathbf{S}_{\text{diab}}^{-1}\boldsymbol{\rho}_{\text{Eth}}(t)\mathbf{S}_{\text{diab}}$.

4
Model Parameterisation

4.1 Single chain model

Basis State	Description
iTT	Intrachain triplet-pair; Two triplet excitations on the same chain.
TT	Interchain triplet-pair; Two triplet excitations on different chains.
EX	Intrachain charge-transfer exciton; Electron and hole separated by more than one ethylene unit on the same chain.
CT	Interchain charge-transfer exciton; Electron and hole on separate chains
FE	Frenkel exciton; Electron and hole localised on the same ethylene unit

Table 4.1: List of basis states, their abbreviations, and their meaning.

The reduced basis model (with parameters summarised in Table 4.2) was used to calculate the excitation energies of the lowest singlet states relevant to singlet fission for lycopene (a chain of 22 C atoms). Table 4.3 compares these results with those of an exact DMRG calculation, from which we see that the model suffers from being able to describe the simpler ionic excitations but not capturing the full correlation in the $2^1A_g^-$ family.

The numerical discrepancies should be expected due to the simplification of the problem we have made. However, the model has been shown to qualitatively reproduce the important underlying physics of the triplet-pair states[63]. It correctly predicts that the $2^1A_g^-$ state is bound although the binding energy ($E(1^5A_g^-)$ –

Parameter	Derived	Fitted
$E_{TT} = 2(V_1 - E_{GS})$	7.36	7.36
$E_{FE} = U - E_{GS}$	7.35	7.65
$E_{EX}(\infty) = U + 2V_1 - 2t_d - 2E_{GS}$	10.16	12.19
$J_{FE}^{intra} = \beta^2(V_1 - 2V_2 + V_3)$	0.37	0.62
$t_T^{intra} = \alpha^2 t_s^2/(E_{EX}(1) - E_T)$	0.86	1.16
$t_{EX} = (\alpha + \beta)^2 t_s/4$	1.07	1.90
$V_{EX-iTT} = \sqrt{3/8}t_s$	1.91	2.55
$V_{EX-FE} = (\alpha + \beta)t_s/\sqrt{8}$	1.53	1.33

Table 4.2: List of derived and DMRG-fitted single-chain model parameters (in eV).

$E(2^1A_g^-)$) of 0.16 eV is significantly lower than the 0.73 eV from the DMRG results. Additionally, the model predicts a triplet-pair weight of 79% for the $2^1A_g^-$ state and 71% for the $1^1B_u^-$ in reasonable agreement with recent DMRG calculations[77]. We therefore choose to keep the model's structure but allow for reparameterisation to better agree with the higher-level DMRG results in order to produce a more accurate effective low-energy model.

The parameter space of the model is enormous, so it is necessary to find independent ways to define each parameter. To begin, we fit the lowest triplet excitations from the DMRG results to a one-particle Hückel-like model,

$$\hat{H}_T = \sum_i \Big(E_T \left|T_i\right\rangle \left\langle T_i\right| - t_T(\left|T_{i\pm1}\right\rangle \left\langle T_i\right| + h.c.)\Big), \tag{4.1}$$

which, for open boundary conditions, has the solution

$$E_j = E_T - 2t_T \cos\Big(\frac{\pi j}{N+1}\Big), \tag{4.2}$$

where $N = 11$ is the number of sites (ethylene units) and j is the pseudo-momentum quantum number. A linear fit of the lowest DMRG triplet excitation energies to equation (4.2) was found to give $E_T = 3.68$ eV and $t_T^{\text{intra}} = 1.16$ eV by least-squares regression.

A similar method was used to find E_{FE} although this has the additional complexity

	$2^1A_g^-$	$1^1B_u^-$	$3^1A_g^-$	$1^5A_g^-$	$1^1B_u^+$	$1^1A_g^+$
Model (raw)	4.05	4.20	4.35	4.21	3.50	3.66
DMRG	2.55	2.86	3.23	3.28	3.00	3.63
Model (fit)	2.68	2.86	3.09	3.12	2.99	3.26

Table 4.3: List of DMRG and reduced-basis model excitation energies (in eV) for a single chain of 22 sites.

j	T (DMRG)	T (fit)	S^+ (DMRG)	S^+ (fit)
1	1.40	1.43	6.44	6.46
2	1.71	1.67	6.60	6.59
3	2.09	2.04	6.81	6.78
4	2.51	2.52	7.02	7.04

Table 4.4: Simple Hückel model fitting of triplet (T) and PH-positive singlet excitation (S^+) energies (in eV) from DMRG.

of both an electron-transfer (via EX) and direct dipolar (J_{FE}) hopping. To isolate these parameters, we performed a DMRG calculation with $t_s = 0$ so that no interethylene hopping was present. We again performed a linear fit to equation (4.2) to find $E_{FE} = 7.65$ eV and $J_{FE}^{\text{intra}} = 0.62$ eV. These results (presented in Table 4.4) show good agreement with the derived excitation energies but require greater intersite terms indicating too great of a localisation of excitations. The relatively large difference in J_{FE}^{intra} might be explained by our model confining this term to nearest-neighbour interactions which is not the case in a full PPP calculation.

There is no method to obtain the remaining parameters (E_{EX}, t_{EX}, V_{EX-iTT}, and V_{EX-FE}) independently. Consequently, we investigated the results of varying each parameter separately with the others taking their new reparameterised values. The results of this parameter scan are given in Figure 4.1 and summarised in Table 4.5.

We found that a significant simultaneous increase in V_{EX-iTT} and t_{EX} is required which results in the lowering of all excitation energies, with the TT levels being most strongly affected. This has the negative effect of narrowing the triplet-pair state spacing which we fix by increasing E_{EX}. A wide parameter space was explore

Parameter	Effect of increase
V_{EX-iTT}	Smaller P(TT) and bandwidth, more strongly bound triplet-pairs.
V_{EX-FE}	Increased P(FE) and decreased FE excitation energies.
E_{EX}	Higher P(TT) and P(FE), increased TT bandwidth, and increased excitation energies.
t_{EX}	Increased bandwidth of charge-transfer states. Decreased P(TT), P(FE) and excitation energies.

Table 4.5: Description of the independent effect of each single-chain parameter as shown in Fig. 4.1. $P(TT)$ is the triplet-pair basis state population in the $2A_g^-$ state and $P(FE)$ is the FE basis state population in the $1B_u^+$ state.

until we found a good match with the DMRG excitation energies while maintaining ~70% TT population in the $2^1A_g^-$ state. Finally, V_{EX-FE} was used to adjust $1^1B_u^+$ into agreement with the DMRG results giving an FE population of 41%, close to the 36% contribution of local ethylene excitations found from exciton-basis valence-bond theory[59]. The final parameters (Table 4.2) provide a good description of the low-energy eigenstates, with all excitation energies around ~0.1 eV of their exact value (Table 4.3).

The greatest problem with this model is its underestimation of the energy spacing between states which no parameter was found to remedy. Higher-order pathways, mediated by multiple excited states, likely contribute to the mobility of excitations which our model cannot readily reproduce. An additional point of interest is that while we accurately replicate the single triplet energies (Table 4.4) this does not guarantee a good model of the $1^5A_g^-$ state which is considered to be made up of two non-interacting triplet excitations confined to a single chain[37]. This is likely a consequence of the model's restriction of triplet excitations to one ethylene site when it has been shown, by investigation of the solitonic structure, that triplets extend over several ethylene units[78]. The underlying issue with the reparameterisation procedure is the use of EX-related parameters to capture all higher-order correlations in both the singly-excited Frenkel excitonic states and the doubly-excited triplet-pair states, whose fundamental nature should require different descriptions. The large

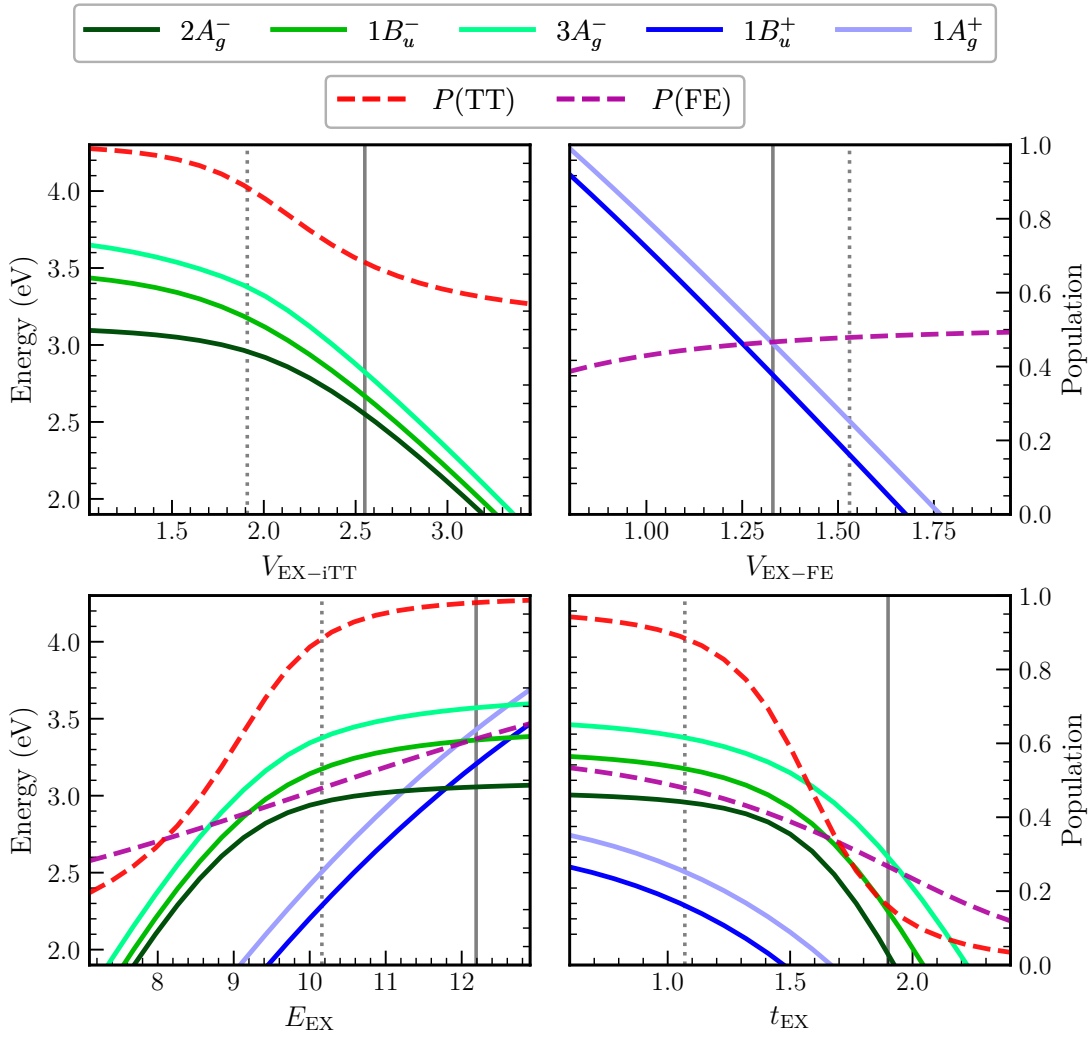


Figure 4.1: Single-chain reduced model parameter scan over V_{EX-iTT}, V_{EX-FE}, E_{EX}, and t_{EX} with all other parameters as defined in Table 4.2. The coloured solid (dashed) curves show the change in the energies (populations). $P(TT)$ is the triplet-pair basis state population in the $2A_g^-$ state, while $P(FE)$ is the FE basis state population in the $1B_u^+$ state. The grey dashed lines indicate the derived value and the solid lines indicate the fitted value of the parameter. Energy levels which do not change are excluded from plots.

renormalisation of t_{EX} required for quantitative results highlights this problem, which may be resolved by enlarging the basis. However, any new basis state would introduce significant complexity to the model and reduce interpretability.

4.2 Dimer Model

All interchain couplings can be related, through our model, to intrachain parameters. We find V_{EX-CT}, V_{TT-CT}, V_{FE-CT} by multiplying their respective intrachain

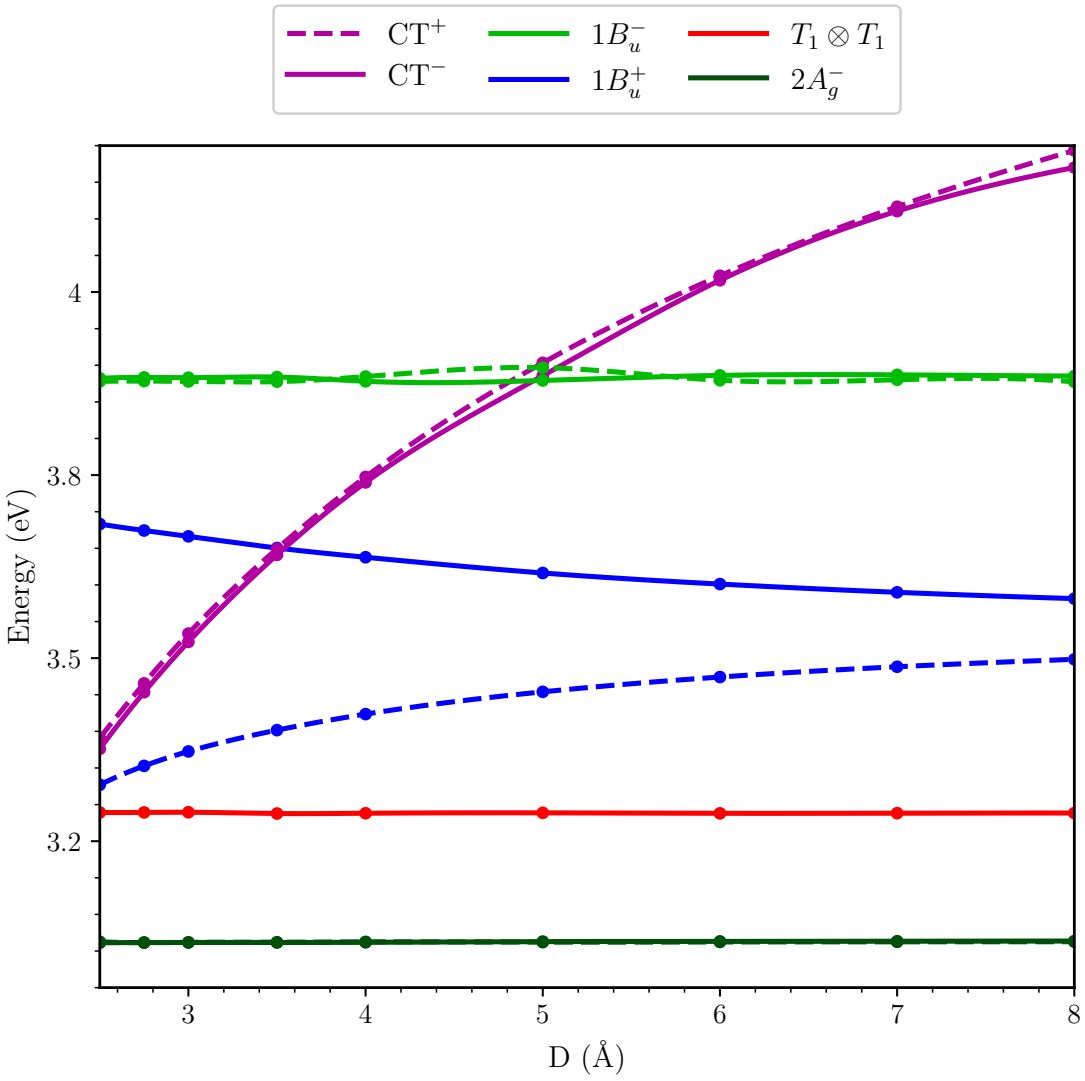


Figure 4.2: Two-chain DMRG calculation of the distance-dependence of excitation energies for vertically stacked chains with a length of 12 C atoms with $t_p = 0$. Solid (dashed) curves indicate +(−) long-axis C_2 symmetry.

equivalents t_{EX}, V_{EX-iTT}, and V_{EX-CT} by t_p/t_s for slipped chains. For vertically stacked chains, the additional electron transfer channel gives an extra factor of two in the multiplier. The exceptions to this rule are t_T^{inter} and J_{FE}^{inter} where the former is derived as,

$$t_T^{\text{inter}} = t_T^{\text{intra}} \left(\frac{t_p}{t_s}\right)^2 \left(\frac{E_{EX}^{NN} - E_T}{E_{CT}^{NN} - E_T}\right), \tag{4.3}$$

for slipped chains while vertically stacked chains gain an additional $2/\alpha^2$ factor.

We now compare our model results to an exact two-chain DMRG calculation on a model dimer system of 12 C atoms per chain. We first investigated the effect on

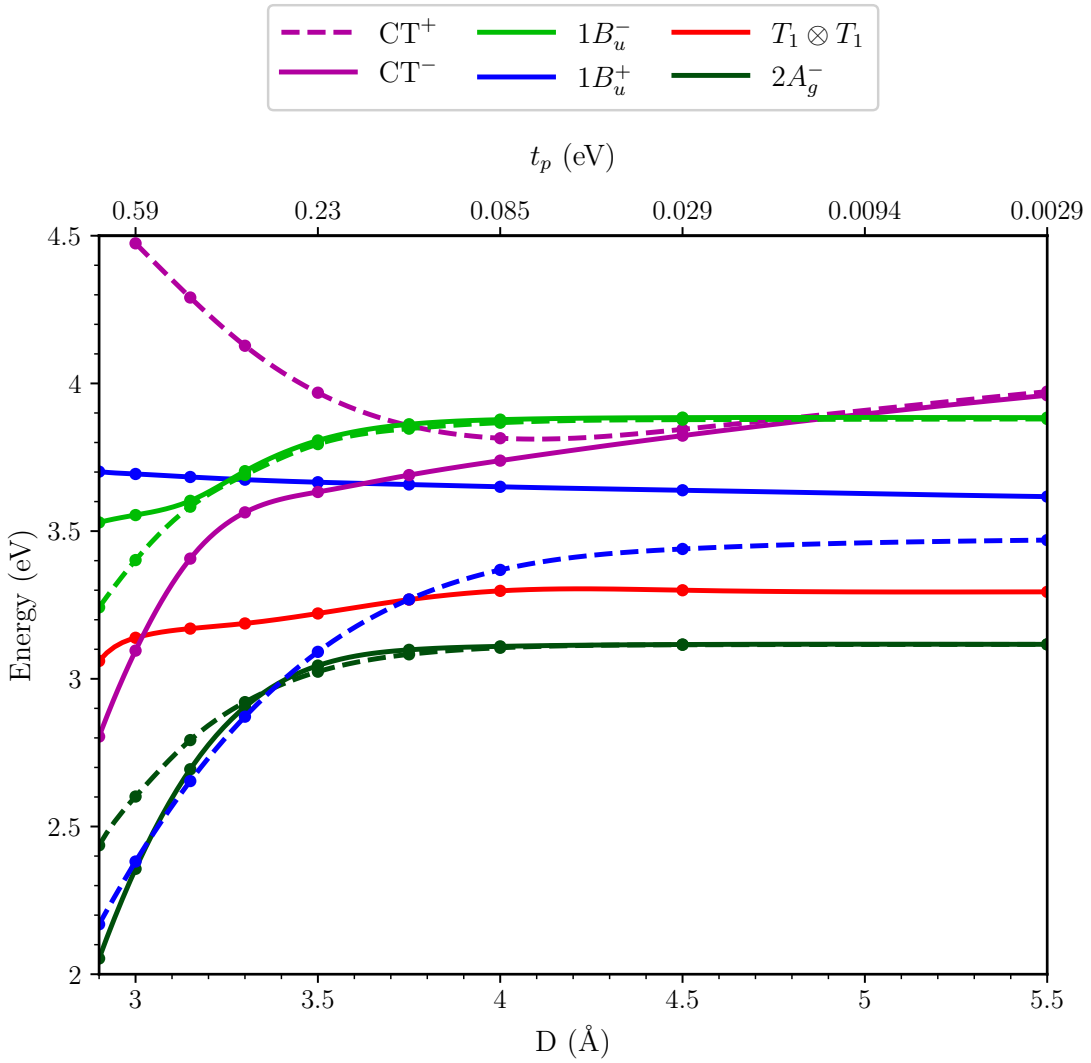


Figure 4.3: Two-chain DMRG exact excitation energies with t_p determined by the Mulliken formula (Eq. 2.18) for vertically stacked chains with a length of 12 C atoms. Solid (dashed) curves indicate +(−) long-axis C_2 symmetry.

the energy levels of changing the interchain distance, D, with $t_p = 0$ (Fig. 4.2). As predicted, we found a splitting between the $1^1B_u^+$ states but none for the triplet-pair states. We observe that the long-axis symmetric/anti-symmetric pair of $1^1B_u^+$ states are evenly split from the single-chain barycentre due to dipolar coupling. We performed a similar calculation for $N = 22$ C atoms with $D = 3.5$ Å chosen to match previous studies[32]. This gave a dipolar splitting of 0.15 eV that required setting $J_{FE}^{\text{inter}} = 0.21$ eV to reproduce in the reduced model which we now adopt. Additionally, we see the presence of a new TT state with energy equal to $2 \times E(\text{T}_1)$

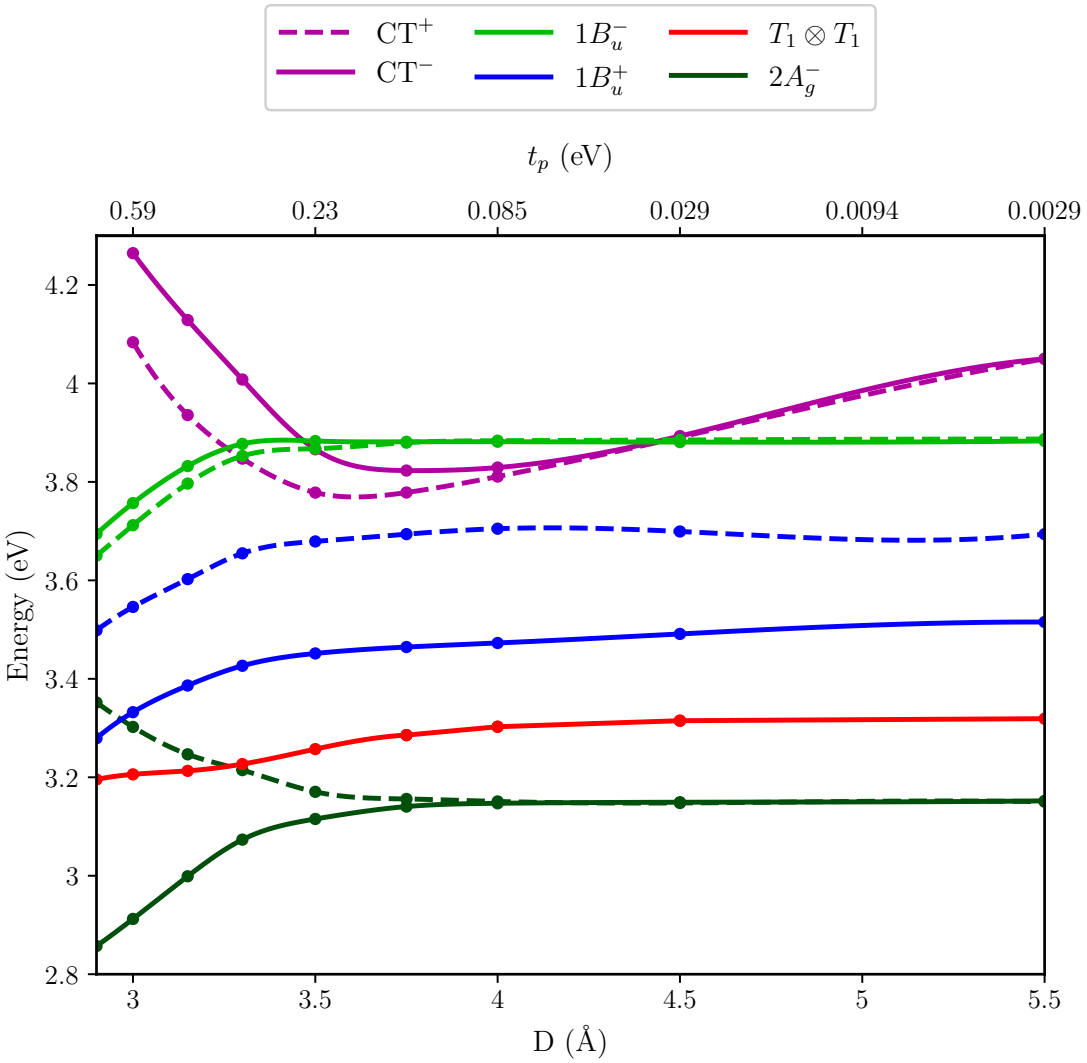


Figure 4.4: Two-chain DMRG exact excitation energies with t_p determined by the Mulliken formula (Eq. 2.18) for slip-stacked chains with a length of 12 C atoms. Solid (dashed) curves indicate $+(-)$ C_2 symmetry.

as well as states whose energy strongly depends on the interchain separation which we assign as charge-transfer states.

We then performed further exact calculations but with t_p as defined by the Mulliken formula (Eq. 2.18) for $p_\sigma - p_\sigma$ overlap (Fig. 4.3). As predicted from our model, we see that the dark anti-symmetric long-axis $1^1B_u^+$ combination interacts with the CT^+ charge-transfer state while the bright combination is unaffected. We also see no coupling of TT and CT states, with CT^- following the same curve as in the $t_p = 0$ case.

Furthermore, performing the same calculations with a slip-stacked geometry (Fig. 4.4) gives results that are easily interpreted by our model. Firstly, we see that both of the CT states mix with other states in this geometry, as predicted by the presence of a new TT-CT coupling (Eq. 2.31). Additionally, we see the competition between the dipole-driven splitting of $1^1B_u^+$ states and the mixing of the bright state with CT states which results in the energy of the bright state shifting down relative to its uncoupled value as interchain separation decreases.

The results of our model for chains at a separation of $D = 3.5$ Å ($t_p = 0.23$ eV as per Eq. 2.18) are presented in Figure 4.5 where we introduce an interchain parameter, τ, which acts as an additional multiplier on top of t_p/t_s to account for any problems in our assumption that interchain couplings are well represented by their intrachain equivalents. Our results closely match the relationships in the DMRG calculations, indicating that we have captured the most important interchain couplings with reasonably accurate magnitudes. Our underestimated Frenkel exciton bandwidth can be seen in the presence of the $1^1A_g^+$ state (second dashed FE curve) which is too rapidly reduced in energy in our model, but this state is not involved in the physics of singlet fission and so it is of little concern. Additionally, in the slip-stacked geometry we see that with $\tau = 1$ the bright FE state has fallen below the dark FE state due to its mixing and repulsion by a higher-lying CT state. As we did not observe this behaviour in the DMRG calculations, we proceed with $\tau = 0.8$ where the state ordering better matches that found in the shorter-chain DMRG calculations.

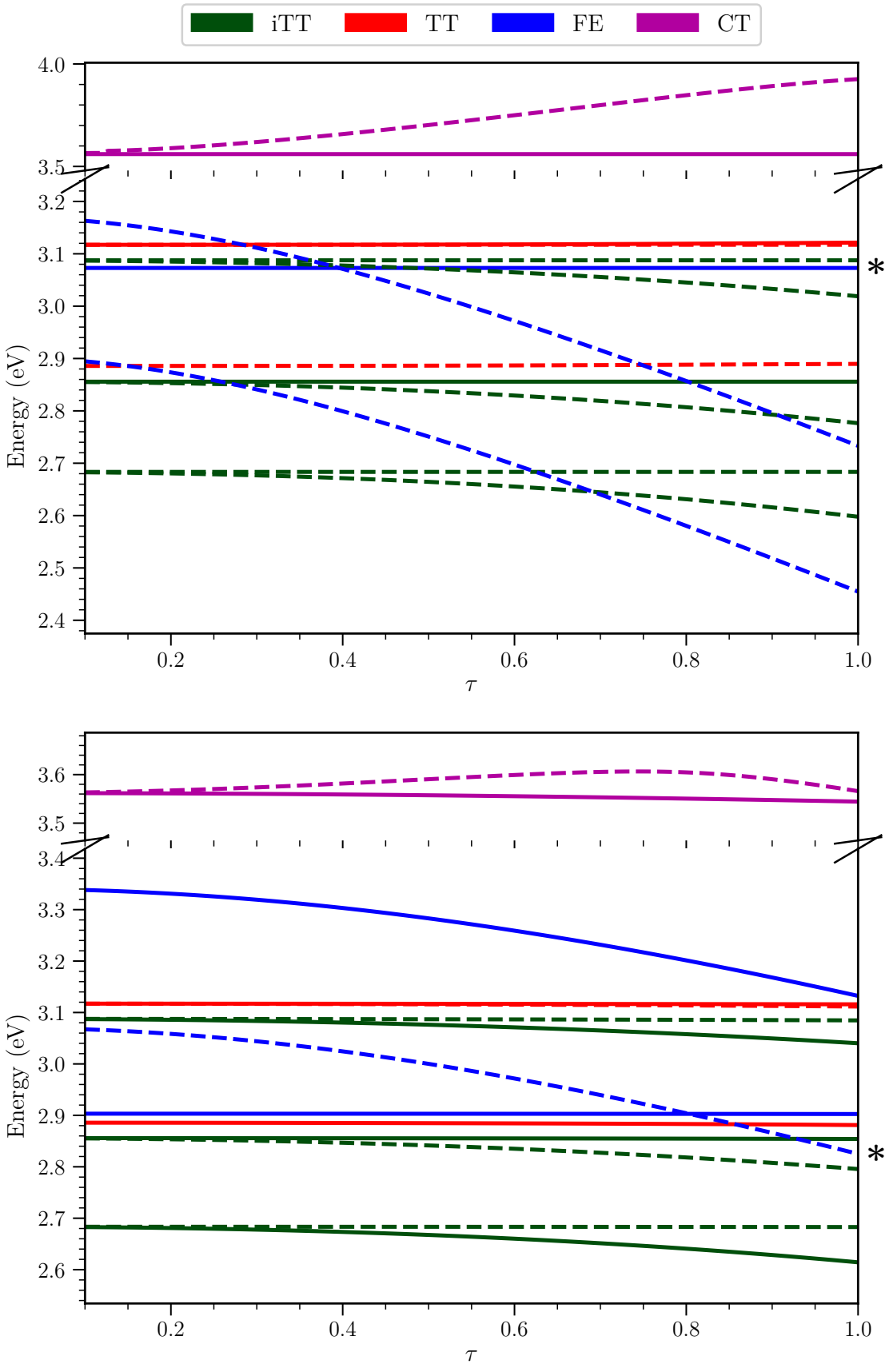


Figure 4.5: Model energies for 2 chains of 22 atoms at a separation of 3.5 Å against τ for vertically stacked (top) and slip-stacked (bottom) chains. Curve colour denotes the dominant character of the eigenstate. Solid (dashed) curves indicate +(−) long-axis C_2 symmetry (top) or overall C_2 symmetry (bottom). The bright state is marked by a *.

5 Dynamics Simulations

With our model constructed and appropriately parameterised, we now present the results of our dynamical simulations on lycopene dimer model aggregates in both vertical and slipped geometries.

5.1 Unitary Evolution

To begin, we perform unitary evolution according to the Liouville-von Neumann equation (Eq. D) with the procedure outlined in Section 3.2.

5.1.1 Breaking Particle-Hole Symmetry

We first investigated the effect of particle-hole symmetry breaking, which allows for conversion (via EX/CT states) between the bright Frenkel exciton state and triplet-pair states of the same spatial symmetry (Fig. 5.1). As suggested in previous studies[67], we add a prefactor, η, to the particle-hole symmetry breaking term in Section 2.2.3 to adjust the extent of PH symmetry breaking. We found that increasing this prefactor results in unrealistic population of high-energy adiabatic (symmetry-broken) states that the model does not describe well. We therefore use a value of $\eta = 0.45$ to avoid this while still giving reasonable conversion between particle-hole symmetry sectors. With only PH-symmetry broken, the only conversion is from $1B_u^+$ to states of B_u^- symmetry, predominantly the intrachain triplet-pair

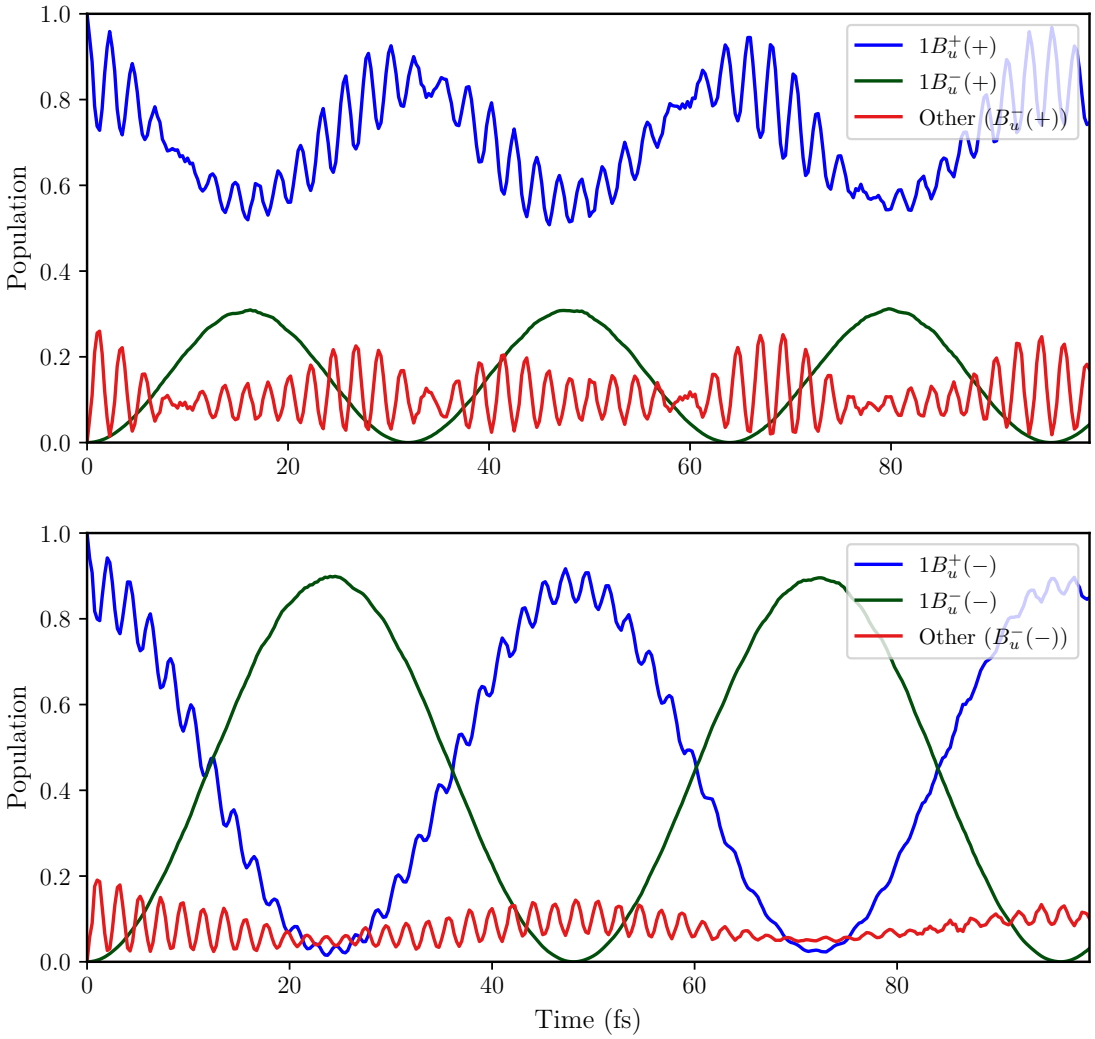


Figure 5.1: Diabatic eigenstate populations during unitary evolution following the procedure of Section 3.2 for vertically stacked chains with $\tau = 1.0$ (top) and slip-stacked chains with $\tau = 0.8$ (bottom). $(+)/(-)$ indicates long-axis C_2 symmetry (top) or overall C_2 symmetry (bottom).

$1B_u^-$. This conversion was found to happen on a slower timescale with greater amplitude in the slip-stacked geometry compared to the vertically stacked as the $1B_u^+ - 1B_u^-$ energy gap is smaller in the former (Fig. 2.7).

5.1.2 Breaking Spatial Symmetry

To allow for conversion into the lowest-lying interchain triplet-pair eigenstate ($T_1 \otimes T_1 = {}^1A_g^-$), C_2 symmetry must be broken as the bright state has opposite short-axis symmetry. We first investigated the effect of structural disorder as described in Section 2.2.3. Without breaking C_2 symmetry, we found very low TT population in

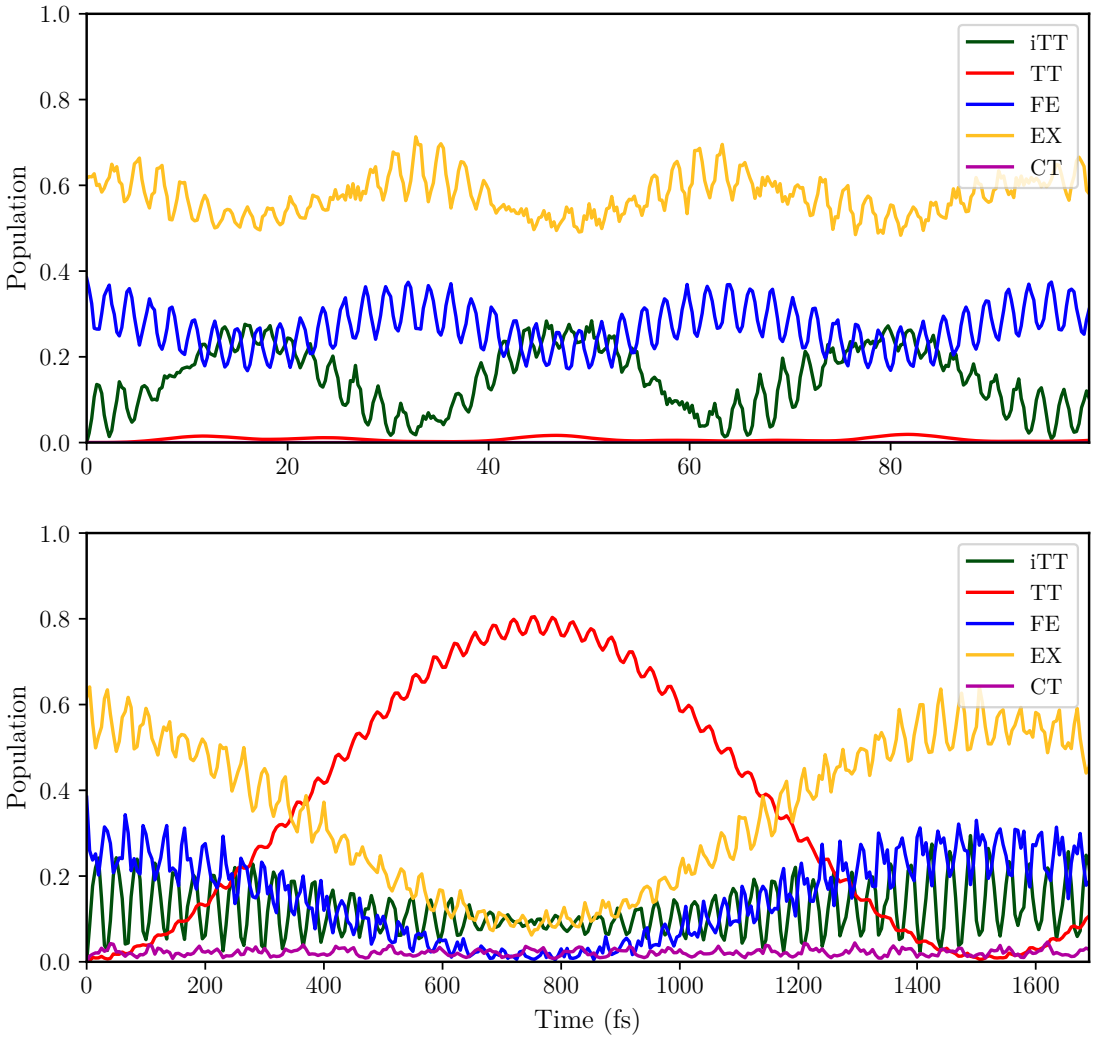


Figure 5.2: Basis state population during unitary evolution of vertically stacked chains with $\tau = 1.0$ and no C_2 symmetry breaking (top) or with C_2 symmetry breaking with $\sigma_d = 0.3$ Å (bottom).

the vertically stacked geometry as only the $T_1 \otimes T_2 = {}^1B_u^-$ interchain state can be accessed by symmetry-allowed processes. This weak mixing of the $T_1 \otimes T_2$ triplet-pair with $1B_u^-$ is due to the relatively large ~0.3 eV energy gap compared with the small interchain triplet hopping coupling term. However, upon applying a C_2 symmetry breaking term with $\sigma_d = 0.3$ Å (allowing fluctuations of interchain distance from $D = 3.5$ Å) we found strong conversion of the bright state into triplet-pairs (Fig. 5.2) with a return period of 1500 fs. In the diabatic view (Fig. 5.3), we observe quickly oscillating bright $1^1B_u^+ \rightarrow 1^1B_u^-$ internal conversion with the C_2 symmetry breaking term then allowing the intrachain triplet-pair $1B_u^-$ state to mix with the interchain

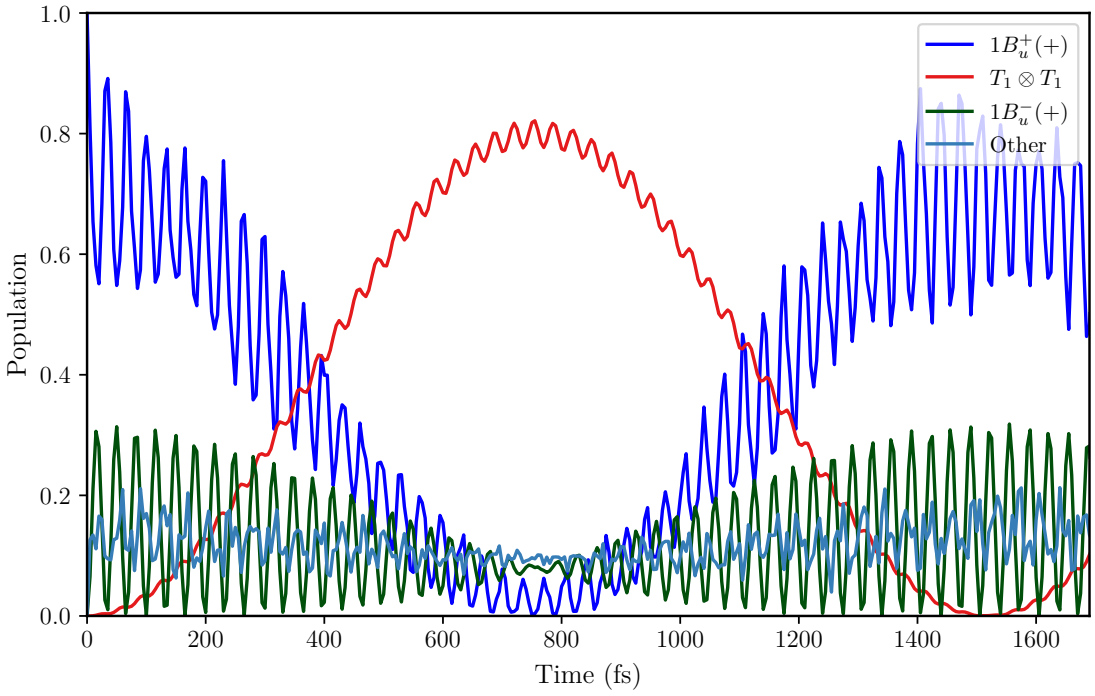


Figure 5.3: Diabatic eigenstate population during unitary evolution of vertically stacked chains with $\tau = 1.0$ and C_2 symmetry breaking with $\sigma_d = 0.3$ Å.

triplet-pair ($T_1 \otimes T_1$) state along the mechanism shown in Figure 1.2d.

In sharp contrast, the slip-stacked geometry was found to give a much lower transient TT population that never reached more than 10%. In other studies, it has been suggested that the features present in the slip-stacked geometry would be more conducive to singlet fission than those in vertically stacked chains[79]. In particular, the presence of CT basis states in both the bright state and the triplet-pair state should provide a superexchange path for the process (Fig. 1.2b). Within our parameter regime, we did not observe this as the derived TT-CT coupling term was found to be relatively small with the lowest TT state having only 0.4% CT character at $\tau = 1.0$. This is because a TT basis state may only couple with a CT basis state if the triplets are located on neighbouring ethylene units on different chains which accounts for only $1/N$ of the possible arrangements of triplets over two chains where N is the number of ethylene units. In contrast to the $\mathrm{iTT} - \mathrm{EX}$ coupling, the much smaller value of V_{TT-CT} does not give rise to binding of the

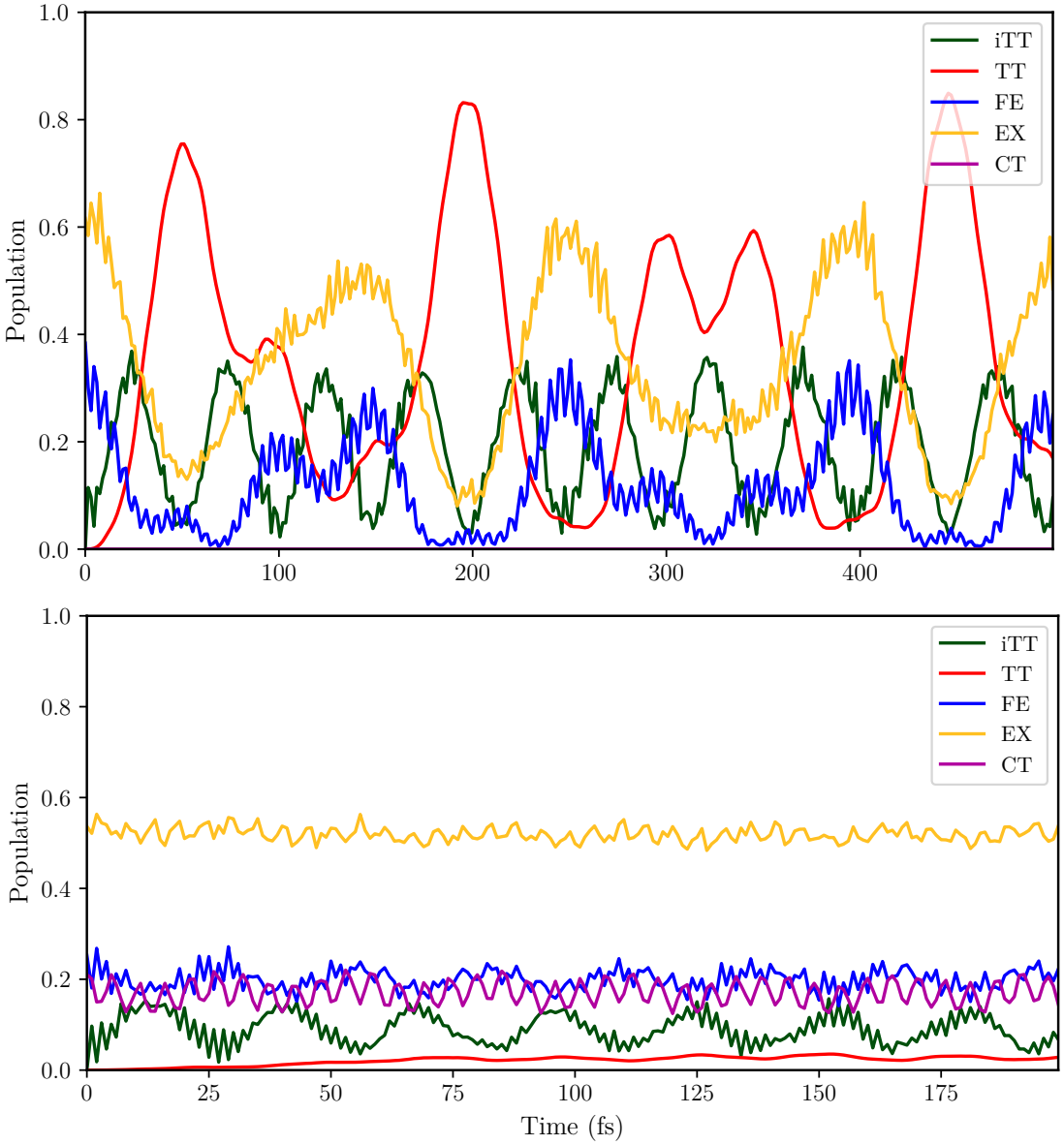


Figure 5.4: Basis state population during unitary evolution of vertically stacked chains with $\tau = 1.0$ (top) and slip-stacked chains with $\tau = 0.8$ (bottom) with vibronic coupling term between $1B_u^-$ and $2A_g^-$.

triplets. Additionally, as described in Section 2.2.2, the transfer integrals between ethylene units on different chains in the slip-stacked geometry are all around half as large as in the vertically stacked arrangement because they are connected by only one overlapping orbital in the former. Although each ethylene unit in the slip-stacked geometry is able to hop to two ethylene units on the other chain (compared to just one for vertically stacked chains), we found that this does not compensate for the

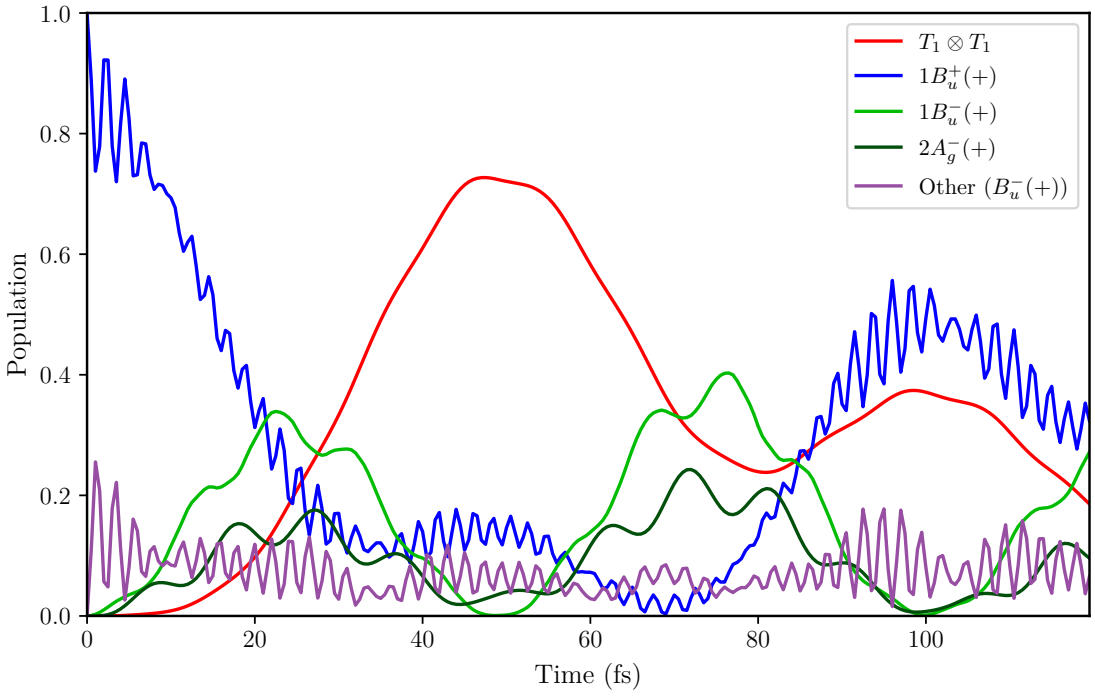


Figure 5.5: Diabatic eigenstate population during unitary evolution of vertically stacked chains with $\eta = 0.45$ and $\tau = 1.0$ with vibronic coupling term between $1B_u^-$ and $2A_g^-$. $(+)/(-)$ indicates long-axis C_2 symmetry.

reduced unit-to-unit transfer integral. Therefore, interchain hopping processes are weaker as a whole in this geometry and so SF is less favourable.

5.1.3 Vibronic Coupling

Another symmetry breaking mechanism is vibronic coupling, which we implement as described in Section 2.2.4. For vertically stacked chains, we find almost complete conversion of the bright state into the lowest energy triplet-pair eigenstate (Fig. 5.4) on a rapid timescale. The diabatic eigenstate populations (Fig. 5.5) show that population of the $\mathrm{T}_1 \otimes \mathrm{T}_1$ interchain TT state occurs after initial population of both the $1B_u^-$ and $2A_g^-$ states which are vibronically coupled. Microscopically, the bright state is made up of FE and EX basis states, the latter of which provides access to the $1B_u^-$ state via the particle-hole breaking term. The $1B_u^-$ state is then vibronically mixed with the $2A_g^-$ state. This is of the same symmetry as the lowest triplet-pair state which can be accessed by interchain triplet hopping. The ~100 fs return period

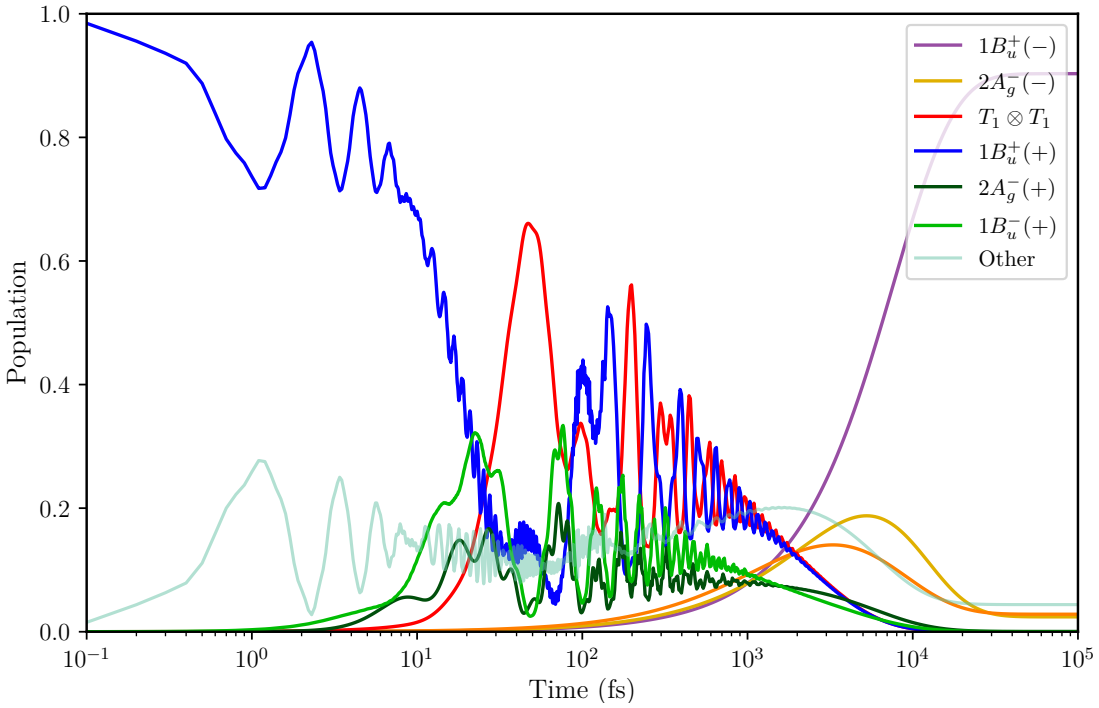


Figure 5.6: Diabatic eigenstate population during time evolution of vertically stacked chains with $\tau = 1.0$ and vibronic coupling term between $1B_u^-$ and $2A_g^-$ under the Redfield equation. $(+)/(-)$ indicates long-axis C_2 symmetry.

for conversion of the bright state into triplet-pairs found by this mechanism is much faster than the 1500 fs period from C_2 symmetry breaking via structural disorder.

We again found very little TT population in the slip-stacked geometry, confirming that for our parameters there is no CT-mediated mechanism.

5.2 Dissipative Dynamics

To understand how these calculations fit into the real process, we performed simulations of the system in contact with a bath according to the Redfield equation, as outlined in Section 2.3.2. In the unitary simulations, only vertically stacked chains showed promise for singlet fission, so we limit our investigation to this geometry. In dissipative simulations, the bath does not respect any symmetries of the system and thus allows population to transfer from any eigenstate to any other according to the energy gap between states and the density of bath phonon modes. The secular approximation to the Redfield equation guarantees that in the long-time

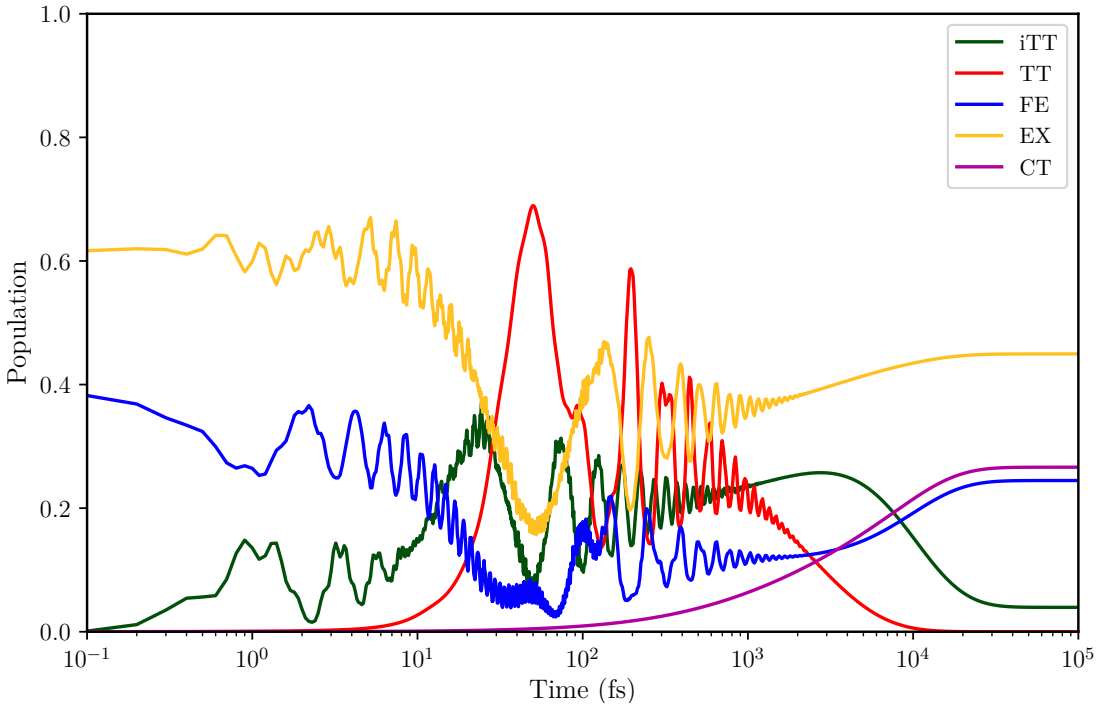


Figure 5.7: Basis state population during time evolution of vertically stacked chains with $\tau = 1.0$ with vibronic coupling term between $1B_u^-$ and $2A_g^-$ under the Redfield equation.

limit the population will reach the Boltzmann thermal distribution which, in our model, is unphysical due to the lack of an explicit ground state. The final state will therefore always be the dark Frenkel exciton $1^1B_u^+$ $(-)$ as this is the lowest excited state in our model (Fig. 4.5).

5.2.1 Vibronic Coupling

With this in mind, we focus on the short term effects (< 10 ps) and present the dissipative simulation under vibronic coupling in Figure 5.6. The early dynamics are dominated by unitary evolution but population of the initial bright state and triplet-pair state is reduced by half within 600 fs. Before thermalisation, we observe several beats in which the $T_1 \otimes T_1$ triplet-pair state is the most populated diabatic eigenstate. However, the model has no mechanism for triplets to move apart once the triplet-pair state is populated and so we observe annihilation and recombination into the lower energy intrachain triplet-pair diabats. The timescale for conversion of the $1B_u^+$ into $1B_u^-$ (within ~100 fs) is in reasonable agreement with transient

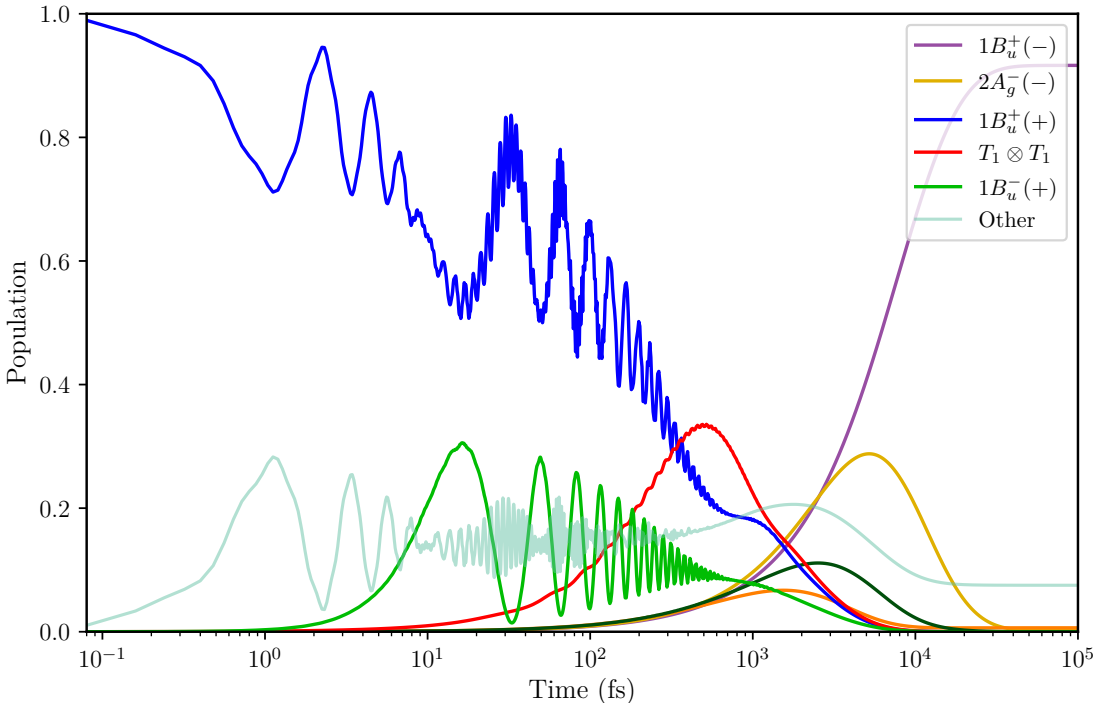


Figure 5.8: Diabatic eigenstate population during time evolution of vertically stacked chains with $\tau = 1.0$ and C_2 symmetry breaking with $\sigma_d = 0.3$ Å under the Redfield equation. $(+)/(-)$ indicates long-axis C_2 symmetry.

absorption experiments[35]. An alternative view, in terms of the population of ethylene basis states, is given in Figure 5.7. This shows the combined conversion of FE basis states into TT and iTT basis states along with the gradual rise of CT basis states as diabats with CT character are thermally populated. We see a rise in CT character on a similar timescale to that found from FSRS experiments[41]. However, this was previously suggested to arise from CT character within the $1B_u^-$ intermediate on the way to triplet-pair production. In contrast to this, we find that the CT population comes from the dark Frenkel exciton $1B_u^+$ $(-)$ which is populated along the relaxation pathway that does not lead to singlet fission.

5.2.2 Breaking Spatial Symmetry

The population of triplet-pair states within 100 fs in our vibronic coupling model is significantly faster than the experimental peak of the ^{1}(TT) signature at 50 ps[35]. The 1.5 ps time period found by unitary evolution with structural disorder (Fig. 5.3) is

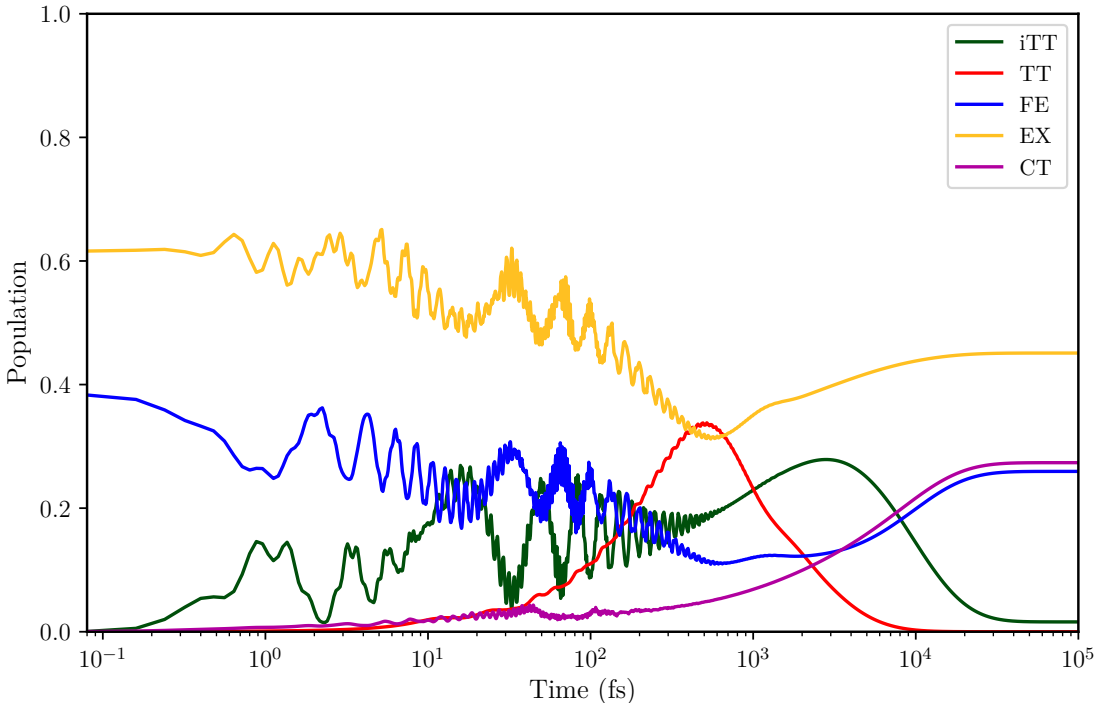


Figure 5.9: Basis state population during time evolution of vertically stacked chains with $\tau = 1.0$ and C_2 symmetry breaking with $\sigma_d = 0.3$ Å under the Redfield equation.

therefore closer to experiment which carries through into our dissipative simulations (Fig. 5.9). As with the vibronic coupling term, we find a similar mechanism of rapid $1B_u^+$ to $1B_u^-$ conversion. However, there is now no strong mixing of $1B_u^-$ and $2A_g^-$ so the interchain triplet $T_1 \otimes T_1$ state is populated directly from the $1B_u^-$ state as the C_2 symmetry restriction that necessitated the mediation of $2A_g^-$ is now lifted. We now find both $2A_g^-$ $(+/-)$ states are populated at later times by reverse triplet of TT back onto a single chain in addition to decay of $1B_u^-$ states that do not undergo interchain triplet hopping. This mechanism is better aligned with transient absorption experiments, where the S_1 signal (from $2A_g^-$) is found to be an alternative decay pathway which is not correlated with the singlet fission pathway. The rise of $T_1 \otimes T_1$ at 1 ps agrees with the beginning of the ^{1}(TT) signal in absorption but the state is found to have a much shorter lifetime due to the lack of diffusion pathways we mentioned previously.

6
Conclusions

We have developed a reduced basis model of the low-energy electronic structure of carotenoid aggregates based on intra- and inter-ethylene excited states. This model was used to investigate the dynamical behaviour of lycopene dimers in both vertically-stacked and slip-stacked geometries, which were found to generate significant differences in the coupling of the underlying basis states.

For vertically stacked chains, it was found that the bright state and all states accessed from it without breaking long-axis symmetry have no interchain charge-transfer character, limiting mechanistic possibilities for singlet fission to involving the intrachain triplet-pair states. This is in contrast to the more commonly discussed superexchange mechanism in polyacenes. We used a particle-hole symmetry breaking term to facilitate conversion into the intrachain triplet-pair $1^1B_u^-$ state. A mechanism to break C_2 symmetry is then required to access the lowest interchain triplet-pair eigenstate. We found best agreement with experiment by using a randomised structural disorder term which allows the interchain transfer integral, t_p, to vary along the chains. Our dissipative simulations showed the $1^1B_u^-$ state convert into the $\mathrm{T}_1 \otimes \mathrm{T}_1$ interchain triplet-pair state within 1 ps. However, with only two chains in the simulation, the triplets were unable to diffuse apart and were found to recombine and relax within 10 ps.

A vibronic coupling symmetry-breaking mechanism was also investigated and found to follow the same intrachain triplet-pair mediated pathway although with timescales that gave worse agreement with experiment. This mechanism could be better understood if the model was expanded to explicitly describe the vibrational energy levels with Frenkel-Holstein terms[48].

The same mechanism was not observed in the slip-stacked geometry where the interchain triplet transfer is weaker. Although the bright state was found to mix strongly with high-lying charge-transfer states, the same was not found to be true for the interchain triplet-pair states and so CT-mediated singlet fission was not observed in our simulations. Our model therefore predicts that the charge-transfer build up observed by Peng et al.[41] arises not from the singlet fission process but from the decay of intermediate states. An alternative explanation may be found by adding a slipping vibration to the model to allow for interchange between the two geometries which would mix CT character into our intermediate states.

In contrast to other studies[32], we did not find the lowest energy eigenstate to be of interchain triplet-pair character, so that singlet fission was not reached in the thermal equilibrium. There may be some structural relaxation around a triplet exciton that we have not included that could account for this and change the order of states[80]. However, accepting our energy ordering does not rule out singlet fission. In a larger aggregate, it is possible that the nearest-neighbour triplet-pairs could diffuse further so that the density of greater-than-nearest-neighbour triplet-pair states would give an entropic driving force that has been under-discussed in the literature[81, 82]. Our simple model is computationally efficient enough to be expanded to larger aggregates and future work should investigate the competition between triplet-pair recombination and diffusion. Additionally, spin-dephasing and zero-field splitting effects could be incorporated into the calculations to give a better simulation of the singlet fission process[40].

Bibliography

(1) Shockley, W.; Queisser, H. J. *Journal of Applied Physics* **1961**, *32*, 510–519.

(2) Nelson, C. A.; Monahan, N. R.; Zhu, X.-Y. *Energy & Environmental Science* **2013**, *6*, 3508.

(3) Singh, S.; Jones, W. J.; Siebrand, W.; Stoicheff, B. P.; Schneider, W. G. *The Journal of Chemical Physics* **1965**, *42*, 330–342.

(4) Hanna, M. C.; Nozik, A. J. *Journal of Applied Physics* **2006**, *100*, 074510.

(5) Smith, M. B.; Michl, J. *Chemical Reviews* **2010**, *110*, 6891–6936.

(6) Smith, M. B.; Michl, J. *Annual Review of Physical Chemistry* **2013**, *64*, 361–386.

(7) Johnson, R. C.; Merrifield, R. E. *Physical Review B* **1970**, *1*, 896–902.

(8) Swenberg, C.; Stacy, W. *Chemical Physics Letters* **1968**, *2*, 327–328.

(9) Rao, A.; Friend, R. H. *Nature Reviews Materials* **2017**, *2*, 17063.

(10) Berkelbach, T. C.; Hybertsen, M. S.; Reichman, D. R. *The Journal of Chemical Physics* **2013**, *138*, 114103.

(11) Lukman, S.; Chen, K.; Hodgkiss, J. M.; Turban, D. H. P.; Hine, N. D. M.; Dong, S.; Wu, J.; Greenham, N. C.; Musser, A. J. *Nature Communications* **2016**, *7*, 13622.

(12) Wang, L.; Zhang, T.-S.; Fu, L.; Xie, S.; Wu, Y.; Cui, G.; Fang, W.-H.; Yao, J.; Fu, H. *Journal of the American Chemical Society* **2021**, *143*, 5691–5697.

(13) Lanzani, G.; Stagira, S.; Cerullo, G.; De Silvestri, S.; Comoretto, D.; Moggio, I.; Cuniberti, C.; Musso, G.; Dellepiane, G. *Chemical Physics Letters* **1999**, *313*, 525–532.

(14) Antognazza, M. R.; Lüer, L.; Polli, D.; Christensen, R. L.; Schrock, R. R.; Lanzani, G.; Cerullo, G. *Chemical Physics* **2010**, *373*, 115–121.

(15) Musser, A. J.; Al-Hashimi, M.; Maiuri, M.; Brida, D.; Heeney, M.; Cerullo, G.; Friend, R. H.; Clark, J. *Journal of the American Chemical Society* **2013**, *135*, 12747–12754.

(16) Polak, D. W.; Andrews, I.; Salvadori, E.; Musser, A. J.; Auty, A.; Chekulaev, D.; Weinstein, J. A.; Heeney, M.; Clark, J. *Journal of the American Chemical Society* **2025**, *147*, 662–668.

(17) Polívka, T.; Sundström, V. *Chemical Physics Letters* **2009**, *477*, 1–11.

(18) Scaccabarozzi, A. D.; Feltri, E.; Mondelli, P.; Rossi, P.; Pallini, F.; Treglia, A.; Petrozza, A.; Beverina, L.; Mattioli, G.; Martin, J.; Luzio, A.; Caironi, M. *ACS Applied Materials & Interfaces* **2026**, *18*, 14056–14066.

(19) Dong, C.; Li, X.-M.; Ma, C.; Yang, W.-F.; Cao, J.-J.; Igbari, F.; Wang, Z.-K.; Liao, L.-S. *Advanced Functional Materials* **2021**, *31*, 2011242.

(20) Frank, H. A.; Bolt, J. D.; Costa, S. M. D. B.; Sauer, K. *Journal of the American Chemical Society* **1980**, *102*, 4893–4898.

(21) Frank, H. A.; McGann, W. J.; Macknicki, J.; Felber, M. *Biochemical and Biophysical Research Communications* **1982**, *106*, 1310–1317.

(22) Llansola-Portoles, M. J.; Redeckas, K.; Streckaité, S.; Ilioaia, C.; Pascal, A. A.; Telfer, A.; Vengris, M.; Valkunas, L.; Robert, B. *Physical Chemistry Chemical Physics* **2018**, *20*, 8640–8646.

(23) Wang, C.; Tauber, M. J. *Journal of the American Chemical Society* **2010**, *132*, 13988–13991.

(24) Nath, M.; Patra, R.; Das, M. *Physical Chemistry Chemical Physics* **2026**, *28*, 4611–4625.

(25) Gradinaru, C. C.; Kennis, J. T. M.; Papagiannakis, E.; Van Stokkum, I. H. M.; Cogdell, R. J.; Fleming, G. R.; Niederman, R. A.; Van Grondelle, R. *Proceedings of the National Academy of Sciences* **2001**, *98*, 2364–2369.

(26) Sutherland, G. A.; Pidgeon, J. P.; Lee, H. K. H.; Proctor, M. S.; Hitchcock, A.; Wang, S.; Chekulaev, D.; Tsoi, W. C.; Johnson, M. P.; Hunter, C. N.; Clark, J. *The Journal of Physical Chemistry Letters* **2023**, *14*, 6135–6142.

(27) Wang, S.; Sutherland, G. A.; Pidgeon, J. P.; Swainsbury, D. J. K.; Martin, E. C.; Vasilev, C.; Hitchcock, A.; Gillard, D. J.; Venkatraman, R. K.; Chekulaev, D.; Tartakovskii, A. I.; Hunter, C. N.; Clark, J. Singlet fission contributes to solar energy harvesting in photosynthesis, arXiv:2411.18801, 2024.

(28) Hestand, N. J.; Spano, F. C. *Chemical Reviews* **2018**, *118*, 7069–7163.

(29) Wang, C.; Schlamadinger, D. E.; Desai, V.; Tauber, M. J. *ChemPhysChem* **2011**, *12*, 2891–2894.

(30) Wang, C.; Berg, C. J.; Hsu, C.-C.; Merrill, B. A.; Tauber, M. J. *The Journal of Physical Chemistry B* **2012**, *116*, 10617–10630.

(31) Musser, A. J.; Maiuri, M.; Brida, D.; Cerullo, G.; Friend, R. H.; Clark, J. *Journal of the American Chemical Society* **2015**, *137*, 5130–5139.

(32) Aryanpour, K.; Shukla, A.; Mazumdar, S. *The Journal of Physical Chemistry C* **2015**, *119*, 6966–6979.

(33) Prodhan, S.; Ramasesha, S. *Physical Review B* **2017**, *96*, 075142.

(34) Quaranta, A.; Krieger-Liszkay, A.; Pascal, A. A.; Perreau, F.; Robert, B.; Vengris, M.; Llansola-Portoles, M. J. *Physical Chemistry Chemical Physics* **2021**, *23*, 4768–4776.

(35) Kundu, A.; Dasgupta, J. *The Journal of Physical Chemistry Letters* **2021**, *12*, 1468–1474.

(36) Pandya, R.; Gu, Q.; Cheminal, A.; Chen, R. Y.; Booker, E. P.; Soucek, R.; Schott, M.; Legrand, L.; Mathevet, F.; Greenham, N. C.; Barisien, T.; Musser, A. J.; Chin, A. W.; Rao, A. *Chem* **2020**, *6*, 2826–2851.

(37) Valentine, D. J.; Manawadu, D.; Barford, W. *Physical Review B* **2020**, *102*, 125107.

(38) Barford, W.; Chambers, C. A. *The Journal of Chemical Physics* **2023**, *159*, 084116.

(39) Barford, W. *The Journal of Physical Chemistry Letters* **2023**, *14*, 9842–9847.

(40) Ichert, A. G.; Barford, W. *Physical Chemistry Chemical Physics* **2025**, *27*, 2371–2380.

(41) Peng, B.; Wang, Z.; Jiang, J.; Huang, Y.; Liu, W. *The Journal of Chemical Physics* **2024**, *160*, 194304.

(42) Magne, C.; Veremeienko, V.; Bercy, R.; Ha-Thi, M.-H.; Arteni, A. A.; Pascal, A. A.; Vengris, M.; Pino, T.; Robert, B.; Llansola-Portoles, M. J. *Scientific Reports* **2025**, *15*, 5593.

(43) Santra, S.; Ray, J.; Ghosh, D. *The Journal of Physical Chemistry Letters* **2022**, *13*, 6800–6805.

(44) Pople, J. A. *Transactions of the Faraday Society* **1953**, *49*, 1375.

(45) Pariser, R.; Parr, R. G. *The Journal of Chemical Physics* **1953**, *21*, 466–471.

(46) Fabian, M. D.; Glaser, N.; Solomon, G. C. *Digital Discovery* **2025**, 10.1039.D5DD00445D.

(47) Jug, K.; Hiberty, P. C.; Shaik, S. *Chemical Reviews* **2001**, *101*, 1477–1500.

(48) Barford, W., *Electronic and optical properties of conjugated polymers*; International series of monographs on physics (Oxford, England) no. 129; Clarendon Press: Oxford, 2005.

(49) Chandross, M.; Mazumdar, S. *Physical Review B* **1997**, *55*, 1497–1504.

(50) Ohmine, I.; Karplus, M.; Schulten, K. *The Journal of Chemical Physics* **1978**, *68*, 2298–2318.

(51) Hudson; Kohler *Chemical Physics Letters* **1972**, *14*, 299–304.

(52) Schulten; Karplus *Chemical Physics Letters* **1972**, *14*, 305–309.

(53) Hudson, B. S.; Kohler, B. E. *The Journal of Chemical Physics* **1973**, *59*, 4984–5002.

(54) Schulten, K.; Ohmine, I.; Karplus, M. *The Journal of Chemical Physics* **1976**, *64*, 4422–4441.

(55) Tavan, P.; Schulten, K. *The Journal of Chemical Physics* **1979**, *70*, 5407–5413.

(56) Tavan, P.; Schulten, K. *Physical Review B* **1987**, *36*, 4337–4358.

(57) Simpson, W. T. *Journal of the American Chemical Society* **1955**, *77*, 6164–6168.

(58) Mazumdar, S.; Chandross, M. In *Primary Photoexcitations in Conjugated Polymers: Molecular Exciton Versus Semiconductor Band Model*; WORLD SCIENTIFIC: 1998, pp 384–429.

(59) Chandross, M.; Shimoi, Y.; Mazumdar, S. *Physical Review B* **1999**, *59*, 4822–4838.

(60) Pleutin, S.; Fave, J.-L. *Journal of Physics: Condensed Matter* **1998**, *10*, 3941–3958.

(61) Pleutin, S.; Fave, J.-L. *Journal of Physics: Condensed Matter* **1999**, *11*, 9629–9645.

(62) Mukhopadhyay, D.; Hayden, G. W.; Soos, Z. G. *Physical Review B* **1995**, *51*, 9476–9492.

(63) Barford, W. *Physical Review B* **2022**, *106*, 035201.

(64) Soos, Z.; Hayden, G. *Chemical Physics* **1990**, *143*, 199–207.

(65) Berencei, L.; Grout-Smith, A.; Poole, J. E.; Barford, W. *The Journal of Chemical Physics* **2019**, *151*, 064120.

(66) Mulliken, R. S.; Rieke, C. A.; Orloff, D.; Orloff, H. *The Journal of Chemical Physics* **1949**, *17*, 1248–1267.

(67) Manawadu, D.; Georges, T. N.; Barford, W. *The Journal of Physical Chemistry A* **2023**, *127*, 1342–1352.

(68) Musser, A. J.; Liebel, M.; Schnedermann, C.; Wende, T.; Kehoe, T. B.; Rao, A.; Kukura, P. *Nature Physics* **2015**, *11*, 352–357.

(69) Georges, T. N.; Summerley, L.; Runeson, J. E.; Barford, W. *The Journal of Physical Chemistry A* **2026**, acs.jpca.6c00402.

(70) Berkelbach, T. C.; Hybertsen, M. S.; Reichman, D. R. *The Journal of Chemical Physics* **2013**, *138*, 114102.

(71) White, S. R. *Physical Review Letters* **1992**, *69*, 2863–2866.

(72) White, S. R. *Physical Review B* **1993**, *48*, 10345–10356.

(73) Schollwöck, U. *Reviews of Modern Physics* **2005**, *77*, 259–315.

(74) Barford, W.; Bursill, R. J.; Lavrentiev, M. Y. *Physical Review B* **2001**, *63*, 195108.

(75) Manawadu, D.; Valentine, D. J.; Barford, W. *The Journal of Physical Chemistry A* **2023**, *127*, 3714–3727.

(76) Kondov, I.; Kleinekathöfer, U.; Schreiber, M. *The Journal of Chemical Physics* **2001**, *114*, 1497–1504.

(77) Ichert, A. G.; Barford, W. Triplet-Pair Character of the 2Ag Dark State of Polyenes, arXiv:2603.08160, 2026.

(78) Bursill, R. J.; Barford, W. *Physical Review Letters* **1999**, *82*, 1514–1517.

(79) Santra, S.; Ghosh, D. *The Journal of Physical Chemistry A* **2025**, *129*, 2738–2744.

(80) Chambers, C. **2023**.

(81) Chan, W.-L.; Ligges, M.; Zhu, X.-Y. *Nature Chemistry* **2012**, *4*, 840–845.

(82) Korovina, N. V.; Chang, C. H.; Johnson, J. C. *Nature Chemistry* **2020**, *12*, 391–398.

(83) Fulde, P., *Electron Correlations in Molecules and Solids*, 3rd ed; Springer Series in Solid-State Sciences Ser v.100; Springer Berlin / Heidelberg: Berlin, Heidelberg, 2002.

(84) Atkins, P. W.; Child, M. S.; Phillips, C. S. G., *Tables for group theory*; Oxford university press: Oxford, 1970.

(85) Breuer, H.-P.; Petruccione, F., *The theory of open quantum systems*, 1. publ. in paperback, [Nachdr.]; Clarendon Press: Oxford, 2009.

(86) May, V., *Charge and Energy Transfer Dynamics in Molecular Systems*, 3rd ed; John Wiley & Sons, Incorporated: Hoboken, 2011.

(87) Nitzan, A., *Chemical dynamics in condensed phases: relaxation, transfer, and reactions in condensed molecular systems*, Second revised edition; Oxford Graduate Texts; Oxford University Press: Oxford, 2024.

(88) Jung, N. J.; Rosati, F.; Rath, G. L.; Wilhelm, F. K.; Schuhmacher, P. K. A mathematical justification to apply the secular approximation to the Redfield equation, arXiv:2505.06786, 2025.

Appendices

A

Solution of the PPP Hamiltonian for Ethylene

The PPP Hamiltonian for ethylene,

$$\begin{aligned}\hat{H} = &- t\sum_{\sigma}(\hat{c}^{\dagger}_{2,\sigma}\hat{c}_{1,\sigma} + \hat{c}^{\dagger}_{1,\sigma}\hat{c}_{2,\sigma}) \\ &+ U[(\hat{N}_{1,\uparrow} - \frac{1}{2})(\hat{N}_{1,\downarrow} - \frac{1}{2}) + (\hat{N}_{2,\uparrow} - \frac{1}{2})(\hat{N}_{2,\downarrow} - \frac{1}{2})] \\ &+ V(\hat{N}_1 - 1)(\hat{N}_2 - 1),\end{aligned} \tag{A.1}$$

can be written in the spin-segregated valence bond basis as

$$\hat{H} = \underset{|T\rangle}{\begin{matrix}S=1\end{matrix}} \begin{pmatrix} V & 0 & 0 \\ 0 & V & 0 \\ 0 & 0 & V \end{pmatrix} \otimes \underset{|FE\rangle \quad |C\rangle \quad |I\rangle}{\begin{matrix}S=0\end{matrix}} \begin{pmatrix} U & 0 & 0 \\ 0 & V & -2t_d \\ 0 & -2t_d & U \end{pmatrix}, \tag{A.2}$$

where the basis states are defined in Figure 2.1.

We then diagonalise within the singlet subspace to get $|GS\rangle$, the intramonomer correlated ground state, and $|X\rangle$ (as defined in Fig. 2.3) where

$$E_{GS} = \frac{U + V_1}{2} - \epsilon, E_X = \frac{U + V_1}{2} + \epsilon \tag{A.3}$$

with

$$\epsilon = \frac{1}{2}\sqrt{(U - V_1)^2 + 16t_d^2} \tag{A.4}$$

and

$$\begin{aligned}\alpha &= \frac{1}{2}\sqrt{\frac{2\epsilon + U - V_1}{\epsilon}} \\ \beta &= \sqrt{1 - \alpha^2},\end{aligned} \tag{A.5}$$

which define the contributions to the ground state of the ionic basis state, $|I\rangle$, and the covalent basis state, $|C\rangle$, where

$$\begin{aligned} \lim_{U\to\infty} \alpha &= \frac{1}{\sqrt{2}}, \\ \lim_{U\to 0} \alpha &= 1. \end{aligned} \tag{A.6}$$

For realistic PPP parameters (Table 2.1), $\alpha^2 \approx \frac{2}{3}$, $\beta^2 \approx \frac{1}{3}$.

B

Super-Exchange Triplet Hopping

In our model, we consider triplet basis state hopping via a superexchange mechanism where the connecting charge-transfer states are taken to be virtual and thus able to be folded into the hopping term via a Wolf-Schrieffer transformation[83].

First, we separate the triplet exciton subspace into a low energy $|T\rangle$ sector and a high energy $|CT\rangle$ sector, with $CT = 1 - T$, and define projection operators $\hat{P}_T$ and $\hat{P}_{CT}$ that project a state vector onto these respective subspaces.

$$\hat{P}_T|\Psi\rangle = |\Psi_T\rangle, \hat{P}_{CT}|\Psi\rangle = |\Psi_{CT}\rangle. \tag{B.1}$$

Projecting $\hat{P}_T$ onto the energy eigenvalue equation gives,

$$\hat{P}_T\hat{H}|\Psi\rangle = E|\Psi_T\rangle. \tag{B.2}$$

Inserting the identity, $\hat{\mathbf{1}} = \hat{P}_T^2 + \hat{P}_{CT}^2$ gives

$$\begin{aligned} &\hat{P}_T\hat{H}(\hat{P}_T^2 + \hat{P}_{CT}^2)|\Psi\rangle = E|\Psi_T\rangle, \\ &\hat{P}_T\hat{H}\hat{P}_T|\Psi_T\rangle + \hat{P}_T\hat{H}\hat{P}_{CT}|\Psi_{CT}\rangle = E|\Psi_T\rangle, \\ &\hat{H}_{TT}|\Psi_T\rangle + \hat{H}_{TCT}|\Psi_{CT}\rangle = E|\Psi_T\rangle. \end{aligned} \tag{B.3}$$

Combine with the expression from similarly projecting $\hat{P}_{CT}$,

$$\hat{H}_{CTCT}|\Psi_{CT}\rangle + \hat{H}_{CTT}|\Psi_T\rangle = E|\Psi_{CT}\rangle, \tag{B.4}$$

to give

$$\hat{H} = \hat{H}_{TT} - \hat{H}_{TCT}\frac{1}{\hat{H}_{CTCT} - E}\hat{H}_{CTT}. \tag{B.5}$$

Then considering the CT subspace as a perturbation to the T subspace, take $E = E_T$ and $\hat{H}_{CTCT} = E_{CT}$ to find the effective triplet Hamiltonian

$$\hat{H}_{eff} = \hat{H}_{TT} - \frac{\hat{H}_{TCT}\hat{H}_{CTT}}{E_{CT} - E_T}. \tag{B.6}$$

Finally, noting that $\hat{H}_{TCT} = (\hat{H}_{CTT})^\dagger = \alpha t_s$ (with α defined as in App. A), we arrive at the superexchange hopping integral,

$$t_T = \langle T; i+1|\hat{H}|T; i\rangle = -\frac{\alpha^2 t_s^2}{E_{CT} - E_T}. \tag{B.7}$$

C

Character Table for the C_{2h} Point Group

Here we provide, for reference, the character tables of the point groups relevant to this thesis[84]. We consider carotenoid chains as possessing C_{2h} symmetry noting that electronic states transform only as A_g and B_u.

C_{2h}	E	$C_2(z)$	σ_{xz}	σ_{yz}		
A_g	1	1	1	1	R_z	x^2, y^2, z^2, xy
B_g	1	-1	1	-1	R_x, R_y	xz, yz
A_u	1	1	-1	-1	z	
B_u	1	-1	-1	1	x, y	

We additionally consider carotenoid dimers which may possess greater symmetry but, for simplicity, we refer to them by their equivalent C_{2h} point group plus the character of any additional C_2 symmetry elements.

D
The Redfield Equation

The exact time evolution of the density operator of a system (S) coupled to an external bath (B) with Hamiltonian,

$$\hat{H} = \hat{H}_S \otimes \hat{\mathbf{1}}_B + \hat{\mathbf{1}}_S \otimes \hat{H}_B + \hat{H}_{SB}, \tag{D.1}$$

is described by the Liouville-von Neumann equation,

$$\frac{\partial \hat{\rho}}{\partial t} = -\frac{i}{\hbar}[\hat{H}, \hat{\rho}]. \tag{D.2}$$

The system's reduced density matrix (the operator $\hat{\rho}$ in a particular basis) is found by tracing over the environment's degrees of freedom,

$$\frac{\partial \hat{\rho}_S(t)}{\partial t} = -\frac{i}{\hbar} Tr_B[\hat{H}(t), \hat{\rho}(t)]. \tag{D.3}$$

To simplify the problem, we proceed in the interaction picture,

$$\hat{\rho}^I(t) = U_I(t)\hat{\rho}U_I^\dagger(t), \tag{D.4}$$

where $U_I(t) = \exp\Big(+i\hat{H}_0 t/\hbar\Big)\exp\Big(-i\hat{H}t/\hbar\Big)$ and Equation (D.3) takes the integro-differential form,

$$\frac{\partial \hat{\rho}_S^I(t)}{\partial t} = -\frac{i}{\hbar} Tr_B[\hat{H}_{SB}^I(t), \hat{\rho}^I(0)] - \frac{1}{\hbar^2}\int_0^t ds\ Tr_B\Big[\hat{H}_{SB}^I(t), [\hat{H}_{SB}^I(s), \hat{\rho}^I(s)]\Big]. \tag{D.5}$$

D.0.1 Redfield Equation

We then take the first term on the right to be zero and simplify the rest further by making a series of approximations[85, 86]:

1. Born approximation: assume weak system-bath coupling so that $\hat{\rho}_B$ is essentially constant through evolution, $\hat{\rho}^I(t) \approx \hat{\rho}^I_S(t) \otimes \hat{\rho}_B$ and the bath is in thermal equilibrium, $\hat{\rho}_B = \frac{\exp(-\beta H_B)}{\mathcal{Z}}$, giving

$$\frac{\partial \hat{\rho}^I_S(t)}{\partial t} = -\frac{1}{\hbar^2}\int_0^t ds\ Tr_B\Big[\hat{H}^I_{SB}(t), [\hat{H}^I_{SB}(s), \hat{\rho}^I_S(s) \otimes \hat{\rho}_B]\Big]. \tag{D.6}$$

2. Markov approximation: assume bath relaxation occurs much faster than system relaxation so that memory effects (the effect of previous system-bath interactions) can be neglected. Transform the integrand as $\tau = t - s$ so that $\hat{\rho}^I_S(t) \approx \hat{\rho}^I_S(t-\tau)$ and then extend the upper limit to infinity (as long-time correlations contribute little) giving the Redfield equation,

$$\frac{\partial \hat{\rho}^I_S(t)}{\partial t} = -\frac{1}{\hbar^2}\int_0^\infty d\tau Tr_B\Big[\hat{H}^I_{SB}(t), [\hat{H}^I_{SB}(t-\tau), \hat{\rho}^I_S(t) \otimes \hat{\rho}_B]\Big]. \tag{D.7}$$

A more convenient form of Equation (D.7) is found by expanding the coupling in terms of system and bath basis operators,

$$\hat{H}^I_{SB}(t) = \sum_\alpha \hat{S}^I_\alpha(t) \otimes \hat{B}^I_\alpha(t) = \sum_{\alpha,\omega} \exp(-i\omega t)\hat{S}_\alpha(\omega) \otimes \hat{B}^I_\alpha(t), \tag{D.8}$$

where $\hat{S}_\alpha(\omega) = \sum_{a,b} \delta_{\omega, E_b - E_a} S^{ab}_\alpha |a\rangle\langle b|$ and $\hat{B}^I_\alpha(t)$ are spatially uncorrelated operators of a quantum-harmonic bath with correlation function[87],

$$\begin{aligned}\mathcal{B}_{\alpha\alpha}(\tau) &= Tr_B[\hat{B}^I_\alpha(t)\hat{B}^I_\alpha(t-\tau)\hat{\rho}_B] = \langle \hat{B}^I_\alpha(\tau)\hat{B}^I_\alpha(0)\rangle_B \\ &= \frac{\hbar}{\pi}\int_{-\infty}^\infty d\omega \exp(-i\omega\tau) J(\omega)[n(\omega)+1],\end{aligned} \tag{D.9}$$

where $n(\omega)$ is the Bose-Einstein distribution, $n(\omega) = (\exp(\beta\omega)-1)^{-1}$, and $J(\omega)$ is the spectral density of bath phonon modes. We then find that Equation (D.7) becomes

$$\frac{\partial \hat{\rho}^I_S(t)}{\partial t} = \sum_{\omega,\omega'}\sum_\alpha \exp(-i(\omega'-\omega)t)\Gamma(\omega)\left([\hat{S}_\alpha(\omega)\hat{\rho}^I_S(t), \hat{S}^\dagger_\alpha(\omega')] + h.c.\right), \tag{D.10}$$

with

$$\Gamma(\omega) = \frac{1}{\hbar^2}\int_{-\infty}^{\infty} d\tau \exp(+i\omega\tau)\mathcal{B}(\tau) = \frac{2}{\hbar}J(\omega)[n(\omega)+1]. \tag{D.11}$$

Solving the Redfield equation (Eq. D.10) exactly requires working in Liouvillian space where $\dim \mathcal{L} = \dim \mathcal{H}^2$, posing a formidable computational challenge for reasonably large systems. Additionally, the Redfield equation is non-Lindbladian meaning it does not guarantee density-matrix positivity or detailed balance.

D.0.2 The Secular Approximation

These problems are solved by making the secular approximation - neglecting terms where $|\omega - \omega'| \neq 0$ - justified by the rapid oscillations in nonsecular terms that average out to zero[88]. Back in the Schrödinger picture, Equation (D.10) takes the master equation form

$$\frac{\partial\hat{\rho}_S(t)}{\partial t} = -\frac{i}{\hbar}[\hat{H}_S, \hat{\rho}_S(t)] + \hat{\hat{R}}\hat{\rho}_S(t), \tag{D.12}$$

where the secular Redfield dissipator, $\hat{\hat{R}}$, is

$$\hat{\hat{R}}\hat{\rho}_S(t) = \sum_{\omega}\Gamma(\omega)\sum_{\alpha}\left(\hat{S}_\alpha(\omega)\hat{\rho}_S(t)\hat{S}^\dagger_\alpha(\omega) - \frac{1}{2}\left\{\hat{S}^\dagger_\alpha(\omega)\hat{S}_\alpha(\omega), \hat{\rho}_S(t)\right\}\right). \tag{D.13}$$

Projecting onto the system Hamiltonian eigenbasis gives,

$$\frac{\partial\rho_{ab}}{\partial t} = -i\omega_{ab}\rho_{ab}(t) + \sum_{cd} R_{abcd}\rho_{cd}(t), \tag{D.14}$$

where $\omega_{ab} = (E_a - E_b)/\hbar$ and R_{abcd} is the Redfield relaxation tensor,

$$R_{abcd} = \sum_{\omega}\Gamma(\omega)\sum_{\alpha}\left[S^{ac}_\alpha(\omega)S^{db}_\alpha(\omega)^* - \frac{1}{2}\delta_{db}\sum_j S^{aj}_\alpha(\omega)^* S^{jc}_\alpha(\omega) - \frac{1}{2}\delta_{ac}\sum_j S^{dj}_\alpha(\omega)^* S^{jb}_\alpha(\omega)\right]. \tag{D.15}$$

We then take the system-bath coupling to be linear and diagonal between sites[10] so that $\hat{S}_\alpha = |\alpha\rangle\langle\alpha| = \sum_{a,b} U_{a\alpha}U^*_{b\alpha}|a\rangle\langle b|$ and assume a nondegenerate spectrum (and

non-degenerate energy gaps) so that Equation (D.15) becomes

$$\begin{aligned} R_{abcd} &= \sum_{\alpha} \left[|U_{a\alpha}|^2 |U_{c\alpha}|^2 \Gamma(\omega_{ca}) - \frac{1}{2} \sum_i |U_{i\alpha}|^2 \left(\delta_{db} |U_{a\alpha}|^2 \Gamma(\omega_{ai}) + \delta_{ac} |U_{b\alpha}|^2 \Gamma(\omega_{bi}) \right) \right] \\ &= k_{c\to a} - \frac{1}{2} \sum_i (\delta_{db} k_{a\to i} + \delta_{ac} k_{b\to i}), \end{aligned} \tag{D.16}$$

where $k_{a\to b} = \sum_\alpha |U_{a\alpha}|^2 |U_{b\alpha}|^2 \Gamma(\omega_{ba})$ and the time-evolution of the populations, $P_a = \rho_{aa}$, and the coherences, ρ_{ab}, are decoupled and take the Pauli master equation form (with $\mathcal{K}_a = \sum_i k_{a\to i}$),

$$\begin{aligned} \frac{\partial P_a(t)}{\partial t} &= -\sum_c R_{aacc} P_c(t) = \sum_c P_c(t) k_{c\to a} - P_a(t) \mathcal{K}_a, \\ \frac{\partial \rho_{ab}}{\partial t} &= -i\omega_{ab} \rho_{ab} + \sum_{cd} R_{abcd} = -\left(i\omega_{ab} + \frac{1}{2} (\mathcal{K}_a + \mathcal{K}_b) \right) \rho_{ab}. \end{aligned} \tag{D.17}$$

Writing the transfer rate terms in full for $E_a > E_b$ we see the secular Redfield equation guarantees detailed balance,

$$\frac{k_{a\to b}}{k_{b\to a}} = \frac{\Gamma(\omega_{ba})}{\Gamma(\omega_{ab})} = \frac{n(|\omega_{ba}|) + 1}{n(|\omega_{ab}|)} = \exp(\beta \omega_{ab}). \tag{D.18}$$